Tumor-derived pericytes driven by EGFR mutations govern the vascular and immune microenvironment of gliomas

Berta Segura-Collar, María Garranzo-Asensio, Beatriz Herranz, Esther Hernández-SanMiguel, Teresa Cejalvo, Bárbara S Casas, Ander Matheu, Ángel Pérez-Núñez, Juan Manuel Sepúlveda-Sánchez, Aurelio Hernández-Laín, Verónica Palma, Ricardo Gargini and Pilar Sánchez-Gómez

Cancer Res. 2021 Feb 16;canres.3558.2020.

https://doi.org/10.1158/0008-5472.CAN-20-3558

Title

Tumor-derived pericytes, driven by EGFR mutations, govern the vascular and the immune microenvironment of gliomas

Short title

The genetic status of EGFR status governs glioma microenvironment

Authors

Berta Segura-Collar[1], María Garranzo-Asensio[1], Beatriz Herranz[1,2], Esther Hernández-SanMiguel[1], Teresa Cejalvo[1], Bárbara S. Casas[3], Ander Matheu[4,5,6], Ángel Pérez-Núñez[7], Juan M. Sepúlveda-Sánchez[8], Aurelio Hernández-Laín[8], Verónica Palma[3], Ricardo Gargini[1*] and Pilar Sánchez-Gómez[1*]

Affiliations

[1]Neurooncology Unit, Instituto de Salud Carlos III-UFIEC, Madrid, Spain.

[2]Facultad de Medicina de la Universidad Francisco de Vitoria, Madrid, Spain.

[3]Laboratory of Stem Cells and Developmental Biology, Faculty of Sciences, Universidad de Chile, Santiago, Chile.

[4]Cellular Oncology group, Biodonostia Health Research Institute, San Sebastian, Spain.

[5]IKERBASQUE, Basque Foundation for Science, Bilbao, Spain.

[6]CIBERFES, Instituto de Salud Carlos III, Madrid, Spain.

[7]Dto. Neurocirugía, Hospital 12 de Octubre, Univ. Complutense, Madrid, Spain.

[8]Instituto de investigaciones Biomédicas I+12, Hospital 12 de Octubre, Madrid, Spain.

*To whom correspondence should be addressed:

Ricardo Gargini, rgargini@isciii.es

Pilar Sanchez-Gomez, psanchezg@isciii.es

Abstract

The extraordinary plasticity of glioma cells allows them to contribute to different cellular compartments in the tumor vessels, reinforcing the vascular architecture. Recently, it was revealed that targeting glioma-derived pericytes, which represent a big percentage of the mural cell population in aggressive tumors, increases the permeability of the vessels and improves chemotherapy efficiency. However, the molecular determinants of this transdifferentiation process have not been elucidated. Here, we show that mutations in EGFR (epidermal growth factor receptor) stimulate the capacity of glioma cells to function as pericytes in a BMX (bone marrow and X-linked)/SOX9 dependent manner. The subsequent activation of PDGFRβ (platelet derived growth factor receptor beta) in the vessel walls of EGFR mutant gliomas stabilize the vasculature and facilitates the recruitment of immune cells. These changes in the tumor microenvironment confer a growth advantage to the tumors, although it also makes them particularly sensitive to pericyte-targeting molecules such as ibrutinib or sunitinib. In the absence of EGFR mutations, high-grade gliomas are enriched in blood vessels too but they show a highly disrupted blood-brain-barrier due to the decreased BMX/SOX9 activation and pericyte coverage, which lead to poor oxygenation, necrosis and hypoxia. Here, we identify EGFR mutations as key regulators of the glioma-to-pericyte transdifferentiation, highlighting the intricate relation between the tumor cells and their vascular and immune microenvironment. Our results lay the foundations for a vascular dependent stratification of gliomas and suggest different therapeutic vulnerabilities depending on the genetic status of *EGFR*, which defines the vascular and the immune landscape of the tumors.

Keywords

Glioma, EGFR, pericytes, blood-brain barrier (BBB), tumor-microenvironment (TME), immune infiltrate

Introduction

Diffuse gliomas are histologically classified as low and intermediate-grade gliomas (Lower-Grade Gliomas, LGG) (grades two and three) or glioblastomas (GBMs) (grade four) [1]. The poor prognosis of these tumors has been attributed in part to treatment limitations related to the tumor localization, but also to the insufficient knowledge about their physiology.

Florid vascular proliferation and aberrant vasculature are distinctive pathological hallmarks of glioma progression. Four distinct mechanisms of vascularization have been proposed in gliomas: vascular co-option, angiogenesis, vasculogenesis and vascular mimicry. The last one is associated with the plasticity of GBM cells, which can transdifferentiate into endothelial cells (ECs) [2] and pericytes [3, 4]. All these mechanisms are inter-linked and overlapped in the history of gliomas and give rise to an abnormal vascular network, with dilated and tortuous blood vessels (BVs) and poor pericyte coverage, which contributes to the formation of an abnormal blood-brain-barrier (BBB) [5].

Whereas the mechanisms that drive glioma neo-vascularization have been described, the genetic alterations that govern them have not been well established. However, it is known that mutations in the *isocitrate dehydrogenase 1/2* (*IDH1/2*) genes, commonly found in LGG, favor the normalization of the vasculature. IDH mutant (IDHmut) gliomas have smaller BVs and are associated with less hypoxia compared with their wild-type (wt) counterparts [6]. Moreover, we have recently described that the microtubule stabilizer TAU/MAPT is induced in IDHmut gliomas and promotes vascular normalization by opposing EGFR signaling [7]. The *EGFR* gene is amplified in 50 to 60% of IDHwt GBMs and half of these tumors carry the vIII variant (exons 2-7 deletion), which generates a constitutive activation of the receptor´s tyrosine kinase. In addition, missense point mutations in the extracellular domain of the receptor are also commonly found in gliomas [8]. All these mutations confer a higher oncogenic potential to the tumor cells through the increase in their proliferative capacity. Moreover, EGFR activation in

glioma cells promotes STAT3/5 activation and cytokine secretion to modify the microenvironment and thus drives tumorigenesis [9]. This adds to the idea that the genotype of glioma driving cells determines their surrounding stroma. Here, we investigated how alterations in *EGFR* affect the vascular phenotype of gliomas and the implications for the progression of the tumors. Our results show the relevance of the glioma-to-pericyte transdifferentiation, driven by EGFR mutations in shaping the vascular and the immune phenotype of the tumors. The data highlight the intricate relation between the glioma cells and their surrounding stroma.

Materials and Methods

Human samples

Glioma tissues were obtained after patient´s written consent (according to the Declaration of Helsinki) and with the approval of the Ethical Committee at Hospital 12 de Octubre (Madrid, Spain) (CEI 14/023 and CEI 18/024). The primary cell lines (Table S1) belong to the Biobank of that Hospital. Fresh tissue samples were digested enzymatically using Accumax (Millipore) and were maintained in stem cell medium; Neurobasal (Invitrogen) supplemented with B27 (1:50) (Invitrogen); GlutaMAX (1:100) (Invitrogen); penicillin-streptomycin (1:100) (Lonza); 0.4% heparin (Sigma-Aldrich); and 40 ng/ml EGF and 20 ng/ml bFGF2 (Peprotech).

Mouse cell lines

Mouse SVZ cell lines were obtained by retroviral expression of EGFRwt or EGFRvIII in primary neural stem cell cultures obtained from the subventricular zone (SVZ) of p16/p19 ko mice as previously described [10] and they were grown in stem cell medium. After infection, the cells were injected into Nude mice. The tumors that grew were dissociated and the lines SVZ-EGFRwt/amp and SVZ-EGFRvIII were established. Both models express GFP and luciferase as a reporter. The GL261 murine glioma cells were maintained in DMEM plus 10% FBS, 2mM L-glutamine, 0.1% penicillin (100 U/ml) and streptomycin (100 μg/ml).

DNA constructs and lentiviral/retroviral production

Retroviral vectors used were pBabe-EGFRwt (#11011) and MSCV-XZ066-GFP-EGFRvIII (#20737). pLV-Hygro-Luciferase (VectorBuilder #VB150916-10098). Lentiviral vector to express shRNAs were: shCD248 (Sigma #SHCLNG-NM_020404: TRCN00000437821) and shSOX9 (Adgene #40644).

In vitro treatments

Cells were treated with ibrutinib (MedChemExpress, 31976) 5μM, DMSO (control), MG132 (Millipore) 10μM, or different concentrations of dacomitinib (Pfizer, PF-299804).

In vivo assays

Animal experiments were reviewed and approved by the Research Ethics and Animal Welfare Committee at our institution (Instituto de Salud Carlos III, Madrid) (PROEX 244/14 and 02/16), in agreement with the European Union and national directives. Intracranial or subcutaneoous transplantations into Nude mice were establish as previously described [11]. Mice were treated with ibrutinib at 12 mg/kg/day through intraperitoneal injection (i.p.), sunitinib (Selleckchem, S1042) at 6mg/kg/day (i.p.), or dacomitinib (Pfizer, PF-299804) at 15mg/Kg/day (i.p.). For drug preparation ibrutinib was dissolved in 4% DMSO + 10% Hydroxypropyl-β-Cyclodextrin (HP-β-CD), sunitinib was dissolved in 4% DMSO + 10% Polysorbate and dacomitinib was dissolved in 20mM sodium lactate (pH=4) (1,5mg/ml). Control animals were treated with these solvents. For MRI analyses, animals were previously anesthetized using 2 % isofluorane (Isobavet, Schering-Plough) and they were IP injected with 0,1 mL of Gd-DOTA (Dotarem, Guerbet). Images were acquired on a 4,7 T Biospec BMT 47/40 spectrometer (Bruker), equipped with a 6 cm actively shielded gradient system, capable of 450 mT/m gradient strength (Universidad Complutense CAI facility).

Cell sorting

SVZ-EGFRwt/amp and SVZ-EGFRvIII tumors were surgically excised from nude mice and the tissue was dissociated of enzymatic digestion at room temperature with Accumax by 30 min. Samples then were filtered through 70 μm strainers and collected in staining medium (PBS containing 2% BSA). Live tumors cells were discriminated from dead cells using propidium iodide and GFP+ cells were isolated with BD FACS Cell Sorter. Cells were collected into 2 ml staining medium and were recovered by centrifugation for further analysis.

Chicken chorioallantoic membrane (CAM) assay

For in vivo evaluation of the angiogenic inductive potential of SVZ derived conditioned media (CM), a CAM assay was performed as previously reported [12]. Photographs were taken with a digital camera HD IC80 (Leica, Heidelberg, Germany) and the number of vessels within a 6-mm radius of the scaffold were counted to determine the angiogenic score, using ImageJ software (NIH, USA). In each photograph, the diameter of 220 vessels was measured using ImageJ software (NIH, USA).

Inmunofluorescent (IF) and Inmunohistochemical (IHC) staining and quantification

IF and IHC staining was performed as previously described [7] using primary and secondary antibodies described in Table S2. For quantification, slides were scanned at 63X or 40X magnification. The number of BrdU-positive cells per field was counted with Fiji-ImageJ software and normalized with the total number of cells. To quantify the IgG extravasation Fiji-ImageJ software was used. The signal from the endomucin channel was subtracted from the IgG channel. To quantify delocalized pericytes, the signal from the endomucin channel was subtracted from the αSMA channel. For the quantification of the vasculature, we counted the number of dilated vessels per field and CD34 staining with Fiji-ImageJ software. A similar approach was used to count the number of immune cells (CD45 or CD68 positive cells per field). Density measurements of blood vessel density, necrotic area and pericytes coverage,

were performed with ImageJ software (http://rsb.info.nih.gov/ij). Furthermore, in case of the necrotic area we used a score to grade the intensity of the quantified necrosis. To calculate vasculature per random field areas was measured in the intratumoral regions of tumor sections.

Flow cytometry analysis of human tumors

Tumors suspensions were obtained after mechanical and enzymatic disaggregation (Accumax (Merck Millipore) (15 min, room temperature (RT) and filtered through 70μM nylon mesh cell strainer (Fisher Scientific). Erythrocytes were lysed with Quicklysis buffer (Cytognos) and cells were incubated with hFcR Blocking (Miltenyi), previous to antibody (Table S2) incubation (20 min at 4°C in PBS 1% fetal bovine serum (FBS)). Viable cells were labelled with a Fixable Viability Stain (Becton Dickinson) (20 min, RT). The analysis was conducted in a Macsquant10 flow Cytometry (Miltenyi). Lymphoid and myeloid subsets were defined as in [13].

In sillico analysis

The Cancer Genome Atlas (TCGA) GBM, LGG and GBM+LGG dataset was accessed via cBioPortal (https://www.cbioportal.org/), UCSC xena-browser (https://xenabrowser.net) and Gliovis (http://gliovis.bioinfo.cnio.es) for extraction of the data: overall survival, gene´s expression level and the distribution of the different genetic alterations. Kaplan-Meier survival curves were done upon stratification based into low and high groups using expression values from each gene. Significance of differences in survival between groups was calculated using the log-rank test. For the functionality studies we have used "David Gene ontolog" analysis. First, we selected a cluster of 365 genes co-expressed with *SOX9*, using the highest value of the spearman´s correlations. Then, "David gene ontology" analysis associates the expression of this genes with the biological processes involved. The hypoxic-related genes signature included hypoxia and HIF1α pathways genes. Ivy Gap date set analysis (http://glioblastoma.alleninstitute.org/) was used to analyze gene signature enrichment between the different anatomic structures identified in the tumor.

Statistical Analysis

GraphPad Prism 5 software was used for data presentation and statistical analysis. For bar graphs, the level of significance was determined by a two-tailed un-paired Student´s t-test. The difference between experimental groups was assessed by Paired t-Test and one-way ANOVA. For Kaplan-Meier survival curves, the level of significance was determined by the two-tailed log-rank test.. P values < 0.05 were considered significant (*p < 0.05; **p < 0.01; *** p< 0.001; **** p< 0.0001; n.s., non-significant). All quantitative data presented are the mean ± SEM. Precise experimental details (number of animals or cells and experimental replicates) are provided in the figure legends.

Data availability

The authors confirm that the data supporting the findings of this study are available within the article and its Supplementary material.

Additional methodological details are provided in the Supplementary Material.

Results

Stratification of gliomas by the genetic status of IDH and EGFR distinguishes between different vascular phenotypes

We first validated that the transcription of three recognized angiogenic markers (*VEGFA, ANGPT2* and *IGFBP2*) shows a strong inverse correlation with the survival of glioma patients (**S1A-S1C Fig**), even if we consider LGG (**S1D-S1F Fig**) and GBM (**S1G-S1I Fig**) separately. Moreover, the progressive increase in their expression paralleled the evolution of the glioma disease (**S1J-S1L Fig**). We then measured the frequency of mutations (**S1M-S1O Fig**) and copy number amplifications (CNA) (**S1P-S1S Fig**) in the groups with high or low quantities of the three genes. As expected, the frequency of *IDH1* mutations was much higher in the gliomas that contain less angiogenic-related mRNAs. Among the rest of the genes

analyzed, we found a consistent enrichment in mutations and CNA of *EGFR* and *EGFR*-related molecules, like *ELDR* (EGFR long non-coding downstream RNA) or *EGFR-AS1*, in the most angiogenic tumors.

Tumors with alterations in *IDH1/2* and *EGFR* account for almost 90% of all gliomas in the cancer genome atlas (TCGA) cohort, and they show a mutually exclusive pattern, with only a small percentage of IDHmut gliomas harboring *EGFR* gains (**Fig 1A**). In order to relate the vascular features with these genetic alterations in gliomas we classified our own cohort of patient's samples in three groups, IDHmut gliomas, IDHwt gliomas without EGFR mutations (herein called EGFRwt/amp) and IDHwt/EGFRmut gliomas, and we measured the amount of the angiogenic-related mRNAs. As it has been previously described [14], the vasculature of IDHmut tumors was close to normal and there was no overexpression of any of the three angiogenic and vascular markers in these tumors compared to normal brain tissue (**Fig 1B-1D**). Among gliomas, we noticed that there was a gradual increase in the amount of the three mRNAs from the IDHmut to the IDHwt/EGFRmut gliomas, being the IDHwt/EGFRwt/amp group in the middle (**Fig 1B-1D**). This result was consistent with the in silico data (**S2A-S2C Fig**) and with the immunohistochemical (IHC) (**Fig 1E**) and the transcriptional (**Fig 1F, 1G**) (**S2D and S2E Fig**) analysis of CD34 (ECs) and αSMA (pericytes), which showed a gradual increase in the three glioma subgroups. The parameters that changed the most were the vascular density (**Fig 1H**) and the number of dilated BVs (**Fig 1I**), typical of malignant gliomas [15].

Our results suggest that the *IDH-EGFR*-based stratification of gliomas allows the distinction of three different vascular phenotypes, highlighting important differences between gliomas that overexpress wild-type or mutant EGFR, probably related to the increased phosphorylation of the receptor (**S2F Fig**), and the increase in the expression of several angiogenesis-related signatures (**S2G-S2J Fig**) observed in the second group. We narrowed down the set of differentially expressed vascular genes to define a "vascular signature" and we

confirmed its higher expression in EGFRmut compared to EGFRamp glioma patients (**Fig 1J**). Notably, this vascular signature showed a strong correlation with the overall survival of glioma patients (**Fig 1K**).

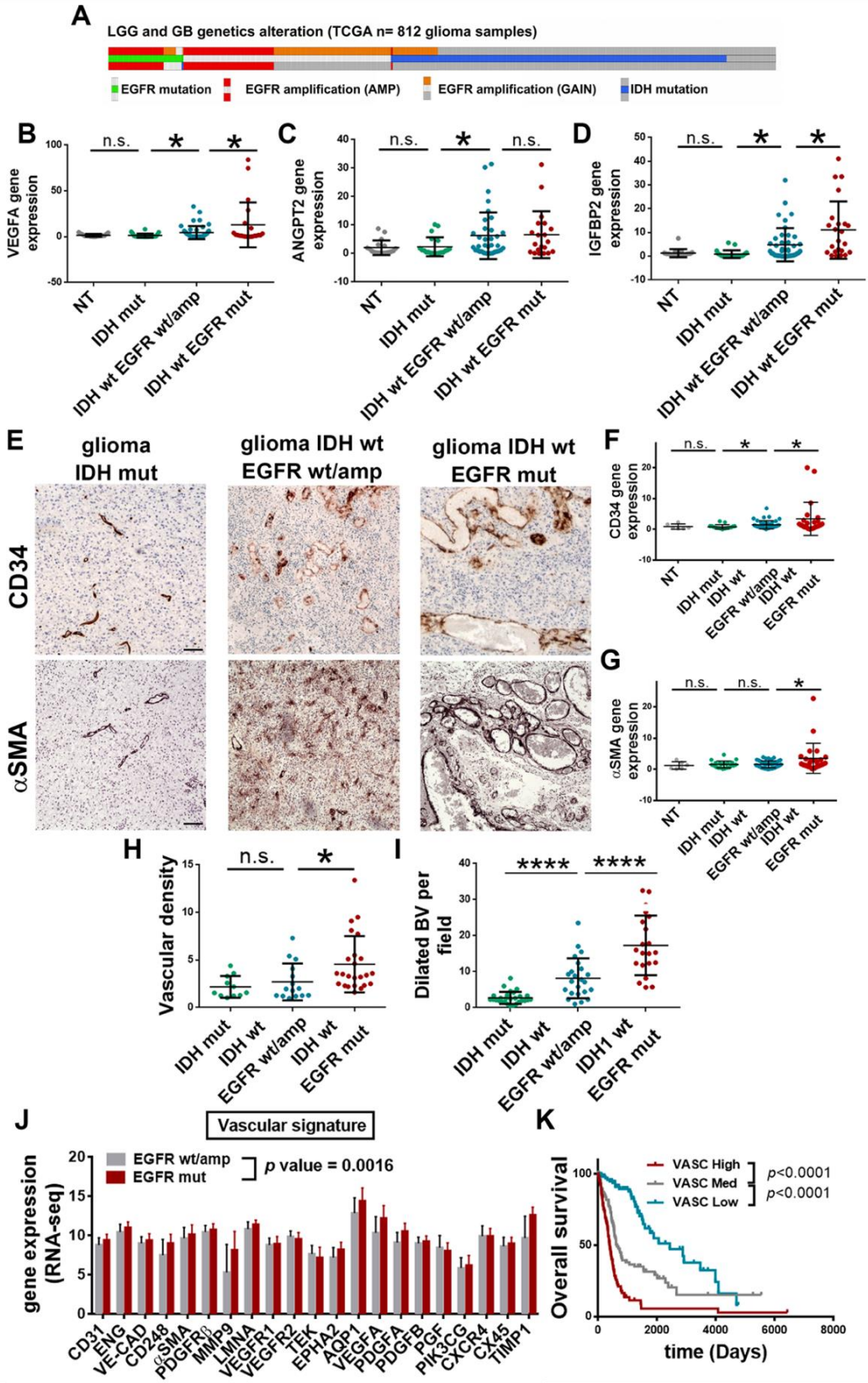

Fig 1. Stratification of gliomas by the genetic status of *IDH-EGFR* distinguishes between different vascular phenotypes. (A) Distribution of somatic nonsilent mutations in *IDH1/2* and *EGFR* in a TCGA (LGG+GBM) cohort (n=663). **(B-D)** qRT-PCR analysis of *VEGFA* (B), *ANGPT2* (C) and *IGFBP2* (D) expression in gliomas (n=93) classified as IDHmut, IDHwt/EGFRwt/amp and IDHwt/EGFRmut. *HPRT* was used for normalization. **(E)** Representative pictures of IHC staining of CD34 (Top) and αSMA (Bottom) in three representative tumors. **(F-G)** qRT-PCR analysis of *CD34* (F) and *αSMA* (G) expression in gliomas (n=93). *HPRT* was used for normalization. **(H)** Quantification of the vascular density in (E) (n=46). **(I)** Quantification of the dilated blood vessels (BVs) in (E) (n=46). **(J)** RNAseq analysis of angiogenesis-related genes in a TCGA (LGG+GBM) cohort (n=319). **(K)** Kaplan-Meier overall survival curves of patients from the TCGA (LGG+GBM) cohort (n=319), stratified into 3 groups based on the expression of the vascular signature. *P ≤ 0.05; ****P ≤ 0.0001. n.s. not significant. Scale bars: 100 μm.

EGFR wt/amp and EGFR vIII cells have different vascular capacities.

The results presented so far suggest important differences in the vascular architecture of gliomas depending on the presence of EGFR mutations. To test the effect of wt or mut EGFR cells in the surrounding vessels, in the absence of any masking effect of concomitant mutations in other genes, we generated two mouse glioma models by transforming SVZ progenitors from p16/p19 ko mice with retrovirus carrying the wt or the vIII isoform of the receptor (**S3A and S3B Fig**). These cells grew in vitro (**S3C Fig**) and they were both very sensitive to dacomitinib (**S3D Fig**), an inhibitor of the receptor´s tyrosine kinase activity [11]. The two mouse cell lines formed subcutaneous tumors, although SVZ-EGFRvIII cells grew faster (**S3E Fig**). Moreover, they were both very sensitive to dacomitinib in vivo (**S3F and S3G**).

Orthotopic implantation of the SVZ models generated gliomas with a high penetrance. Tumor burden was higher after the injection of vIII-expressing cells (**Fig 3A**), which correlates with the worse prognosis of EGFRmut gliomas in comparison with those harboring the wt receptor (amplified or not) (**Fig 3B**). The IHC and the immunofluorescent (IF) analysis of the tumors revealed a higher compact and proliferative growth after EGFRvIII expression (**Fig 3C and 3D**). The vascular density was not significantly different between the two models (**Fig 3E and 3F**) but we observed a strong increase in the size of the vessels in EGFRvIII gliomas (**Fig 3E and 3G**). To obtain an independent confirmation of this observation, we used the CAM assay, which has been widely used to study angiogenesis [16]. Bio-cellulose scaffolds were embedded in VEGFA (as a control) or conditioned media (CM) from SVZ-EGFRwt/amp or SVZ-EGFRvIII cells, and they were layered on top of growing CAMs (**S3H Fig**). Although the CM from both type of cells demonstrated a pro-angiogeneic capacity (**S3I Fig**), the diameters of the vessels formed were larger in the presence of CM from SVZ-EGFRvIII cells compared to their wild-type counterparts (**S3J Fig**). Moreover, we observed that the vascular signature was strongly upregulated in SVZ-EGFRvIII compared to SVZ-EGFRwt/amp tumors (**Fig 3H and 3I**). Notably, some of the top genes in this comparative analysis were linked to pericytic differentiation (*Cd248*) and function (*Timp1*) (**Fig 3I**). Overall, these results confirm the pro-angiogenic function of EGFR signaling in gliomas. Moreover, they suggest that the expression of different isoforms of the receptor have a distinct effect on the vascular microenvironment.

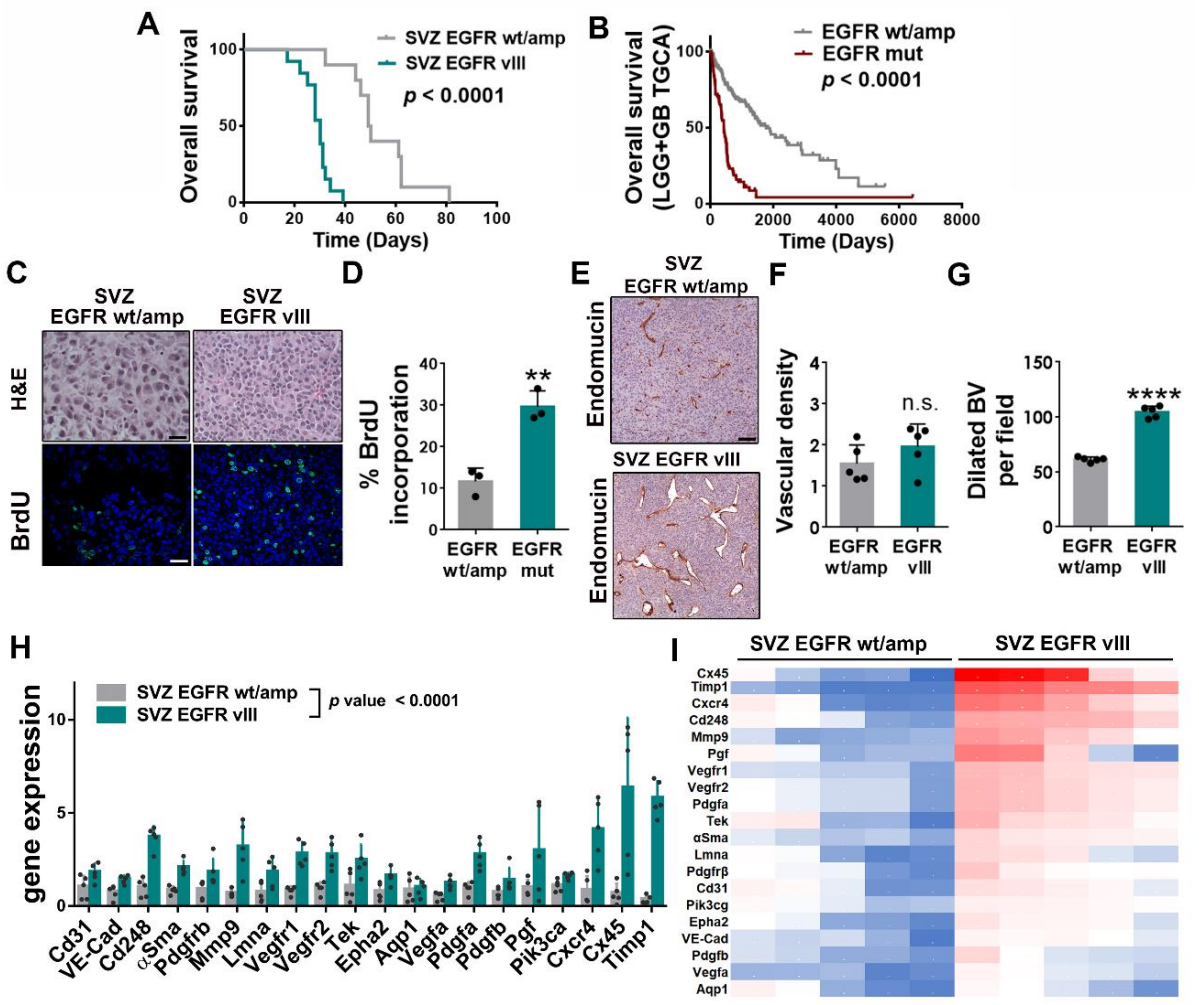

Fig 3. EGFR wt/amp and EGFR vIII cells have different vascular capacities. (A) Kaplan-Meier overall survival curves of mice that were orthotopically injected with SVZ-EGFRwt/amp or SVZ-EGFRvIII cells (n=10). **(B)** Kaplan-Meier overall survival curves of patients from the TCGA cohort (GBM+LGG) separated based on the genetic status of *EGFR* (n=272). **(C)** Representative images of hematoxylin and eosin (H&E) (Top) and BrdU uptake (Bottom) in sections from SVZ tumors. **(D)** Quantification of the percentage of BrdU+ cells in SVZ tumors (n=3). **(E)** Representative images of the endomucin IHC staining of SVZ glioma sections. **(F-G)** Quantification of the vascular density (F) and the number of dilated blood vessels (BVs) (G) in (E) (n=5). **(H)** qRT-PCR analysis of angiogenesis-related genes in SVZ-EGFRwt/amp and SVZ-EGFRvIII tumors. *Actin* was used for normalization (n=5). **(I)** Heat map of gene

expression analysis in H. Red: highest expression. Blue: lowest expression. ** P ≤0.01; ****P ≤0.0001; n.s. not significant; Scale bars: 25 μm (C), 100 μm (E).

EGFRwt/amp expression is associated with a hypoxic phenotype.

To our surprise, the magnetic resonance imaging (MRI) analysis of the grafted mice revealed a cumulative increase in the contrast enhancement of SVZ-EGFRwt/amp compared to SVZ-EGFRvIII injected brains (**Fig 4A and 4B**). We also observed a stronger extravasation of Evans Blue (**S4A Fig**) and IgG (**Fig 4C and 4D**) in SVZ-EGFRwt/amp compared to mutant tumors. These observations suggest that the integrity of the BBB is severely compromised in the former. The disruption of the BBB has been associated with impaired blood perfusion and the formation of hypoxic regions in tumors [17]. Accordingly, HIF1α expression (**Fig 4E**) and the hypoxia-related signature (**Fig 4F**) were higher in SVZ-EGFRwt/amp compared to SVZ-EGFRvIII tumors. This signature was defined using the IvyGAP (Ivy GBM Atlas Project) data-set analysis (**S4B Fig**), selecting the most relevant genes included in hypoxia and HIF1α pathways signatures that were up-regulated in the perinecrotic and pseudopalisading-cell-necrosis tumor zones (**S4C Fig**). Notably, this signature was increased in mesenchymal (MES), compared to classic (CL) or proneural (PN) gliomas (**S4D Fig**) [18]. MES gliomas are characterized by a high frequency of EGFR amplifications (but not mutations) and show a higher overall fraction of necrotic area and a stronger expression of hypoxia-regulated genes compared to the other subtypes [18, 19]. By contrast, tumors harboring EGFR mutations tend to accumulate in the CL subgroup, characterized by a highly proliferative phenotype [18, 20].

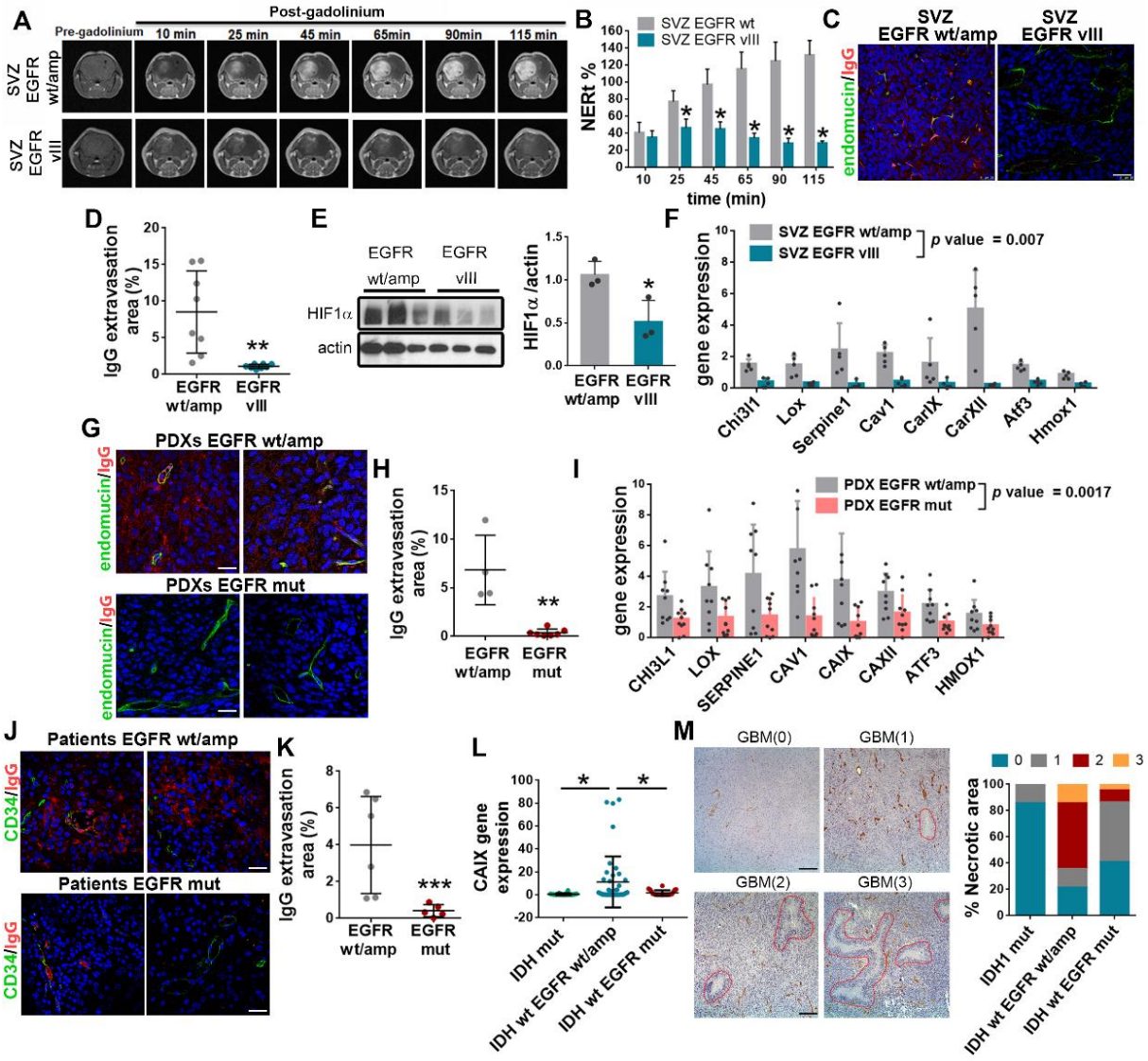

Fig 4. EGFRwt/amp expression is associated with a hypoxic phenotype. (A) Representative T1 contrast enhanced MRI scans of mouse brains containing SVZ tumors at different time points after gadolinium (Gd) injection. **(B)** Quantification of the Gd extravasation in (A) (n=3). NERt: normalized enhancement ratio. **(C)** Representative images of endomucin and IgG IF staining of sections from SVZ tumors. **(D)** Quantification of IgG extravasation on (C) (n=16). **(E)** WB analysis and quantification of HIF1α in SVZ tumors. Actin was used for normalization. **(F)** qRT-PCR analysis of hypoxic-related genes signature in SVZ tumors (n=5). *Actin* was used for normalization. **(G-H)** Representative images (G) and quantification (H) of endomucin and IgG IF staining of sections from PDXs (n=11). **(I)** qRT-PCR analysis of hypoxic-related genes

signature in EGFRwt/amp (n=9) and EGFRmut (n=10) PDXs. *HPRT* was used for normalization (PDXs). **(J)** Representative images of endomucin and IgG IF staining of sections from human glioma samples. **(K)** Quantification of IgG extravasation on (J) (n=10). **(L)** qRT-PCR analysis of *CAIX* expression in human glioma samples. *HPRT* was used for normalization (n=89). **(M)** Representative pictures of the hematoxylin and eosin (H&E) staining of different GBMs. Necrotic areas are highlighted with a red line and the necrotic area score is represented between brackets. The percentage of tumors (n=48) with different necrotic area scores is shown on the right. *P ≤ 0.05; **P ≤ 0.01; ***P ≤ 0.001; Scale bars: 50 μm (C), 25 μm (G, J), 100 μm (M).

We then performed an IF analysis in different orthotopic patient-derived-xenografts (PDXs) that express EGFRwt/amp or EGFRmut (deletions and/or point mutations). We observed the increase in the permeability of IgG in the prior compared to the latter (**Fig 4G and 4H**). This effect was paralleled by an upregulation of the hypoxia-related signature in EGFRwt/amp PDXs (**Fig 4I**). Notably, the extravasation of IgG was also increased in EGFRwt/amp compared to EGFRmut patients´ tumors (**Fig 4J-4K**). Besides, we found a strong increase in the expression of *Carbonic Anhydrase IX (CAIX)*, one of the main HIF1α targets, in IDHwt/EGFRwt/amp gliomas compared to tumors with *IDH* or *EGFR* mutations (**Fig 4L**). IDHmut tumors contain a more "normalized" vasculature without vessel leakage [7] and a reduced extent of necrosis [21]. The histological analysis of the tumor´s sections confirmed these observations (**Fig 4M**). Moreover, it showed an accumulation of necrotic areas in EGFRwt/amp compared to EGFRmut gliomas (**Fig 4M**). These results suggest that the angiogenic signals induced by amplification or overexpression of wt EGFR result in a dense vascular network, but with a severely compromised BBB, a different phenotype to the one

observed in mutant EGFR tumors. This vascular fragility is associated with a less efficient fueling of tumor proliferation and with the appearance of areas of necrosis and hypoxia.

Glioma-derived pericytes stabilize the vasculature in EGFRmut tumors.

SVZ-EGFRvIII tumors showed a highly compact growth, whereas in SVZ-EGFRwt/amp tumors cells appeared detached from each other and from the tumor vessels (**Fig 5A**). It has been shown that pericytic functions can be performed by the highly plastic glioma stem cells, which acquire mesenchymal and mural cell features [3] in a process regulated by EGFR signaling [7]. In agreement with these notions, some tumor cells expressed αSMA in both SVZ glioma models (**Fig 5B**). Furthermore, pericyte-related markers were expressed in GFP+ cells, sorted out after tumor dissociation, independently of the genetic status of *EGFR* (**Fig 5C**). However, we noticed an increased transcription of *αSma* and *Cd248* in SVZ-EGFRvIII tumor cells, compared to their wild-type counterparts (**Fig 5D**). Notably, among the vascular signature, several pericyte-related genes were upregulated in cultured SVZ-EGFRvIII cells (**S5A Fig**), suggesting that they express these markers even in the absence of the microenvironment-derived signals, and that this process is exacerbated in the presence of the mutant isoforms of the receptor. In agreement with these results, there was a significant increase in the expression of human *αSMA* and *CD248* (**Fig 5E**) and in the ratio of tumor pericytes to mouse ECs (**S5B Fig**) in EGFRmut compared to EGFRwt/amp PDXs. By contrast, the transcription of host pericyte genes in all the PDX tested was similar to that of normal mouse brain (**Fig 5E and S5B Fig**). Notably, human endothelial transcripts (*CD31*, *END*) were not overexpressed in the PDXs, independently of the genetic status of *EGFR* (**S5C Fig**). These results suggest that in the presence of EGFR mutations glioma cells have a higher capacity to differentiate into pericytes but not to ECs. Indeed, we found that up to 80% of the αSMA+ cells in a patient´s tumor express the vIII mutation (**S5D Fig**). Moreover, we found an increased

pericyte coverage in mouse (**Fig 5F**) and human (**Fig 5G**) glioma transplants. By contrast, we noticed that the amount of delocalized pericytes (those that were not in close contact with ECs) was higher in wild-type compared to mutant EGFR tumors (**S5E and S5F Fig**).

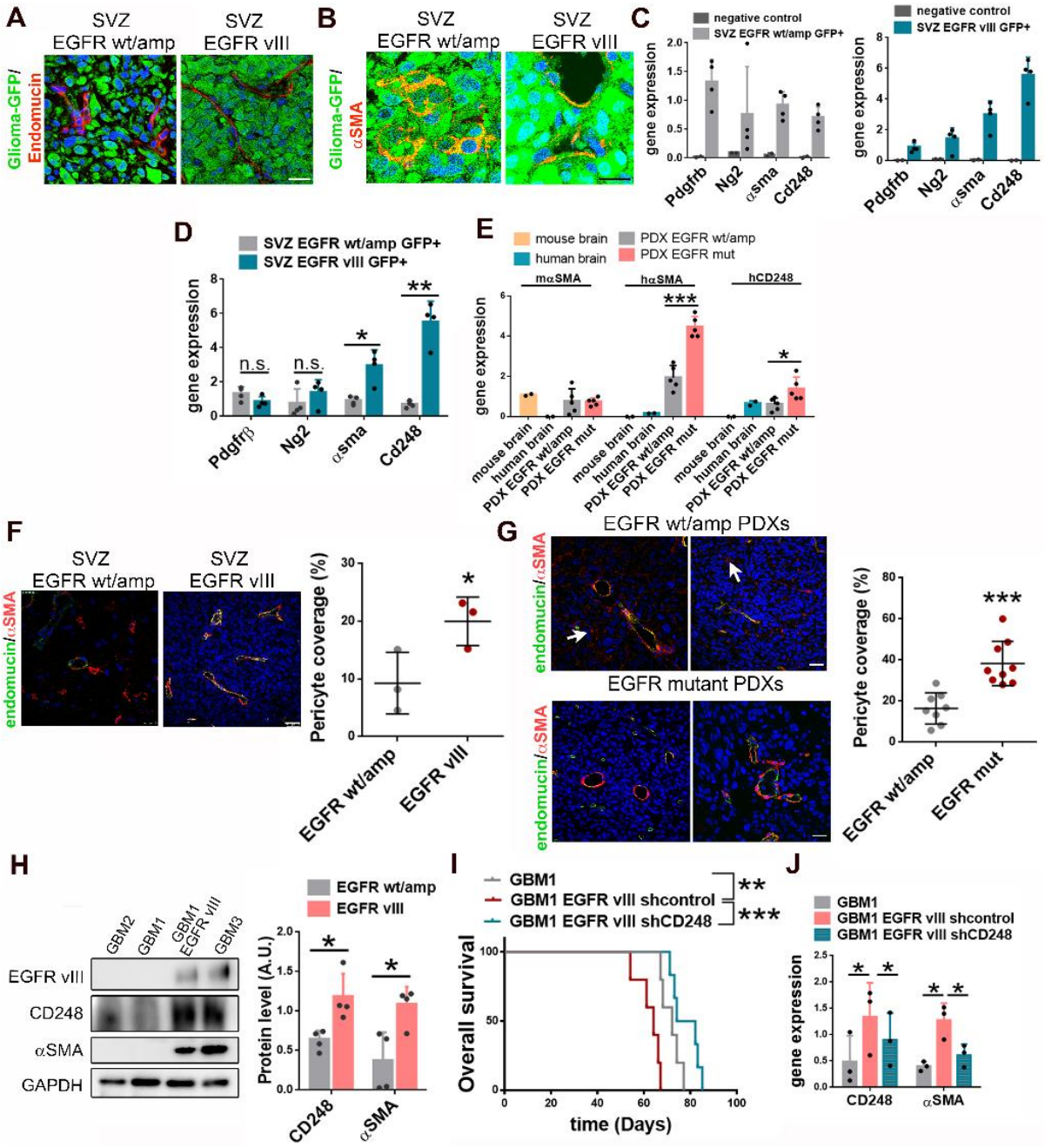

Fig 5. Glioma-derived pericytes stabilize the vasculature in EGFRmut tumors. (A-B) Representative pictures of GFP+ glioma cells and endomucin (A) or αSMA (B) IF staining of sections from SVZ tumors**. (C)** qRT-PCR analysis of pericytic-related genes in GFP+ sorted

cells from SVZ tumors (n=4). Human cDNA was used as negative control. *Actin* was used for normalization. **(D)** Comparative analysis of expression of pericytic markers in tumors from (C). **(E)** qRT-PCR analysis of pericytic–related genes in EGFRwt/amp and EGFRmut PDXs (n=5). Human and mouse tissue were used as control. *HPRT* or *Actin* were used for normalization. **(F-G)** Representative images of endomucin and αSMA IF staining of sections from SVZ gliomas (F) and PDXs (G). Arrows point towards examples of αSMA-positive cell that do not localize close to endomucin+ cells. Quantification of the pericyte coverage is shown on the right of the images (F, n=10). (G, n=8). **(H)** WB and quantification of EGFRvIII, □SMA and CD248 in GBM1 and GBM2 (EGFRwt/amp), GBM1-EGFRvIII, and GBM3 (EGFRamp/mut) cells. GAPDH was used as loading control. **(I)** Kaplan-Meier overall survival curves of mice that were orthotopically injected with GBM1, GBM1-EGFRvIII-shcontrol and GBM1-EGFRvIII-shCD248 (n=6). **(J)** qRT-PCR analysis of *CD248* and *αSMA* in the tumors in (I). *HPRT* was used for normalization (n=3). *****P ≤ 0.05; **P ≤ 0.01; ***P ≤ 0.001; n.s. not significant. Scale bars: 10μm (A-B), 25μm (F-G).

To further study the transdifferentiation function of mutant EGFR, we introduced EGFRvIII in GBM1 cells (EGFRamp). We observed a strong increase in the amount of αSMA and CD248 protein in vitro, similar to the expression observed in GBM3 cells (EGFRamp/EGFRvIII) (**Fig 5H**). Overexpression of the mutant receptor increased the aggressiveness of the GBM1 tumors (**Fig 5I**) and induced a higher transcription of human-specific pericyte genes (**Fig 5J**). Notably, downregulation of *CD248*, a master regulator of pericyte differentiation in malignant solid tumors [22, 23], decreased the aggressiveness of GBM1-EGFRvIII tumors (**Fig 5I**), with a concomitant decrease in the expression of other pericyte makers (**Fig 5J**). Taken together, these results confirm that EGFR mutations promote

the growth of gliomas, at least in part through the increase in the plasticity of the tumor cells, which can work as pericytes and reinforce the stability of the vessels.

EGFR mutations modulate the vascular properties of glioma cells in a BMX and SOX9 dependent way.

EGFR signaling activates transcription factors that drive tumor growth. We performed an *in-silico* analysis in order to find those factors overexpressed in EGFRmut gliomas but with a similar expression in wild-type or amplified *EGFR* gliomas. The best hit was the Sex-determining region Y (SRY)-box 9 (*SOX9*) gene (**S6A Fig**), which has been previously linked to EGFR [24, 25]. We found a strong upregulation of the SOX9 protein (**Fig 6A**) and mRNA (**Fig 6B**) in those PDXs harboring *EGFR* mutations. Similarly, SOX9 was accumulated in SVZ-EGFRvIII allografts, but not in SVZ-EGFRwt/amp or in GL261 (commonly used mouse glioma model) tumors (**S6B Fig**). Furthermore, in the presence of a proteosomal inhibitor the amount of SOX9 was increased in EGFRwt/amp cells but did not change in EGFRmut cells (**Fig 6C**), suggesting the stabilization of the protein in the latter.

SOX9 participates in a variety of functions during development, although it has also been implicated in the regulation of cancer stem cells [26]. Moreover, we found a positive association of *SOX9* with angiogenic processes in gliomas (**Fig 6D**). Downregulation of this protein in GBM3 (EGFRamp/EGFRvIII) (**Fig 6E and 6F**) or in GBM1-EGFRvIII (**S6C and S6D Fig**) cells impaired their orthotopic growth. Notably, the expression of *CD248* and other pericyte-related genes was decreased in GBM3-shSOX9 compared to control tumors (**Fig 6F and S6E Fig**), suggesting that SOX9 mediates the induction of pericyte properties in EGFRmut tumors. In agreement with that, we found a positive correlation between the transcription of *SOX9* and different pericytic-related genes in gliomas (**S6F-S6I Fig**). Notably, we observed a decrease in the pericyte coverage (**Fig 6G**), concomitant with the upregulation of the IgG

extravasation (**Fig 6H**) and the hypoxia-related signature expression (**Fig 6I**) in *SOX9* interfered tumors. These observations reinforce the idea that blockade of the transdifferentiation capacity of EGFRmut GBM cells favors the fragility of the tumor vessels and the subsequent induction of hypoxia, similar to what occurs in tumors over-expressing wild-type EGFR.

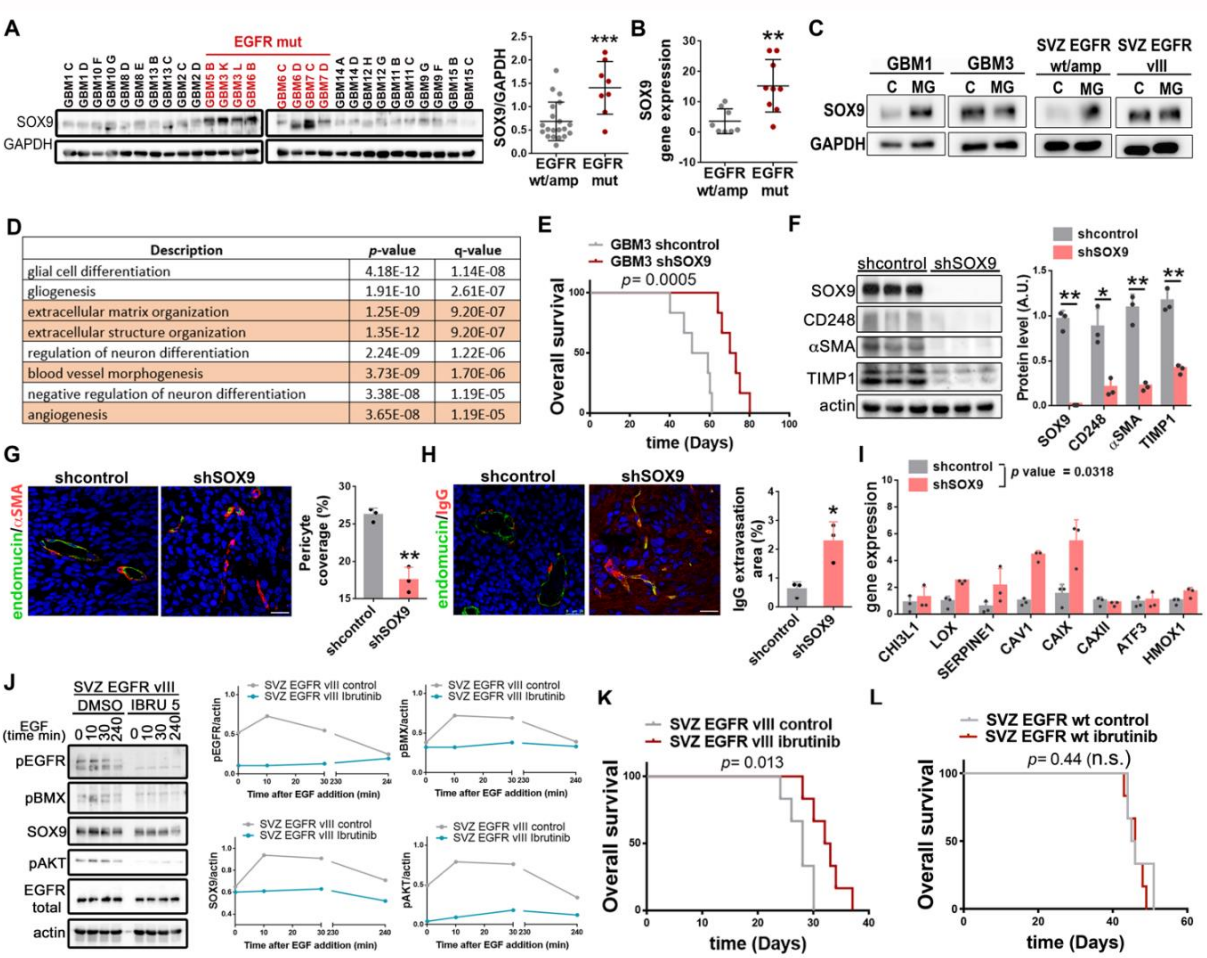

Fig 6. EGFR mutations modulate the vascular properties of glioma cells in a BMX- and SOX9-dependent way. (A) WB analysis and quantification of SOX9 expression in PDXs. GAPDH was used for normalization. **(B)** qRT-PCR analysis of *SOX9* expression in PDXs (n=9). *HPRT* expression was used for normalization. **(C)** WB analysis of SOX9 in EGFRwt/amp cell lines (GBM1 and SVZ) and EGFRvIII cell lines (GBM3 and SVZ) in the absence or in the presence of MG132 (MG) (10µm). **(D)** Gene Ontology Enrichment Analysis performed using David Bioinformatics Resources on the cluster of genes that are positively co-

expressed with *SOX9* in the TCGA (LGG+GB) cohort. **(E)** Kaplan-Meier overall survival curves of mice that were orthotopically injected with GBM3-shcontrol or GBM3-shSOX9 cells (n=6). **(F)** WB analysis and quantification of SOX9, CD248, αSMA and TIMP1 in the tumors in (E) (n=3). Actin was used as loading control. **(G)** Representative images of endomucin and αSMA IF staining of tumors in (E). Quantification of the pericyte coverage is shown on the right (n=3). **(H)** Representative images of endomucin and IgG IF staining of sections from tumors in (E). Quantification of IgG extravasation is shown on the right (n=3). **(I)** qRT-PCR analysis of hypoxic-related genes in the tumors in (E) (n=3). *HPRT* was used for normalization **(J)** WB analysis and quantification of pEGFR, pBMX, SOX9, pAKT and total EGFR in growth factor-starved SVZ-EGFRvIII cells incubated with EGF (100ng/ml) for the times indicated, in the presence of DMSO or Ibrutinib (5μm). Actin was used for normalization. **(K-L)** Kaplan-Meier overall survival curves of mice that were orthotopically injected with SVZ-EGFRvIII cells (K) and SVZ-EGFRwt (L) and subsequently treated with intraperitoneal injections of ibrutinib (12mg/kg/day) (n=6).

A recent study has discovered that the bone marrow and X-linked (BMX) nonreceptor tyrosine kinase is highly expressed in glioma derived-pericytes but not in normal mural cells in the brain [27]. However, the upstream signals have not been described yet. In order to test if EGFR signaling could be connected to BMX activation in glioma cells, we performed an in vitro analysis in response to EGF. Stimulation with the ligand induced EGFR activation and signaling in SVZ-EGFRvIII (**Fig 6J**) and SVZ-EGFRwt/amp (**S6J Fig**) cells. However, it only stimulated BMX phosphorylation in the presence of the mutation (**Fig 6J and S6J Fig**). Moreover, we observed an accumulation of SOX9 protein at short times after EGF stimulation in EGFRvIII (**Fig 6J**) but not in EGFRwt/amp cells (**S6J Fig**). Ibrutinib, a dual BMX/BTK (Bruton's tyrosine kinase) inhibitor that impairs tumor-to-pericyte transdifferentiation [27],

blocked BMX stimulation and SOX9 accumulation in response to EGF in SVZ-EGFRvIII cells (**Fig 6J**). EGFR and AKT phosphorylation were impaired in the presence of ibrutinib in both types of cells (**Fig 6J and S6J Fig**). However, ibrutinib impaired tumor growth of SVZ-EGFRvIII cells (**Fig 6K**), but not their wild-type counterparts (**Fig 6L**). The reduced tumor burden was paralled by a reduced phosphorylation of EGFRvIII and BMX, as well as a reduction in the expression of *SOX9* and pericyte markers in the treated tumors (**S6K Fig**). These results suggest that EGFRmut-BMX signaling induces the accumulation of SOX9 protein and the subsequent formation of tumor-derived-pericytes, increasing the aggressiveness of EGFRmut gliomas but rendering these tumors sensitive to ibrutinib.

PDGFRβ activation in the pericytes of EGFR mutant gliomas is responsible for the entrance of immune cells into the tumors

In order to further characterize the vascular phenotype of wild-type and mutant EGFR gliomas, we compared the expression of several important signaling pathways in angiogenic and vascular development in the SVZ models. We observed a strong increase in the levels of phospho-PDGFRβ (platelet derived growth factor receptor-β), with no differences in the amount of total PDGFRβ, phospho-AKT or β-catenin in the tumors expressing EGFRvIII (**S7A Fig**). This increase was detected as well in several EGFRmut PDXs (**S7B Fig**) and human tumors (**Fig 7A**) compared to the wild-type tumors. In both type of samples, we found a strong correlation between the phosphorylation of EGFR and PDGFRβ (**Fig 7B and S7B Fig**). Activation of the latter in response to the secretion of PDGF ligands by endothelial cells is crucial for the proper integration of pericytes in the vessel walls [28]. In agreement with that, we detected specific phospho-PDGFRβ labelling adjacent to the endothelium in several EGFRmut PDXs (**S7C Fig**). Notably, PDGFRβ activation was not observed in SVZ-EGFRvIII

cells in vitro or in GL261 tumors (**S7A Fig**), which show many vascular abnormalities, even though they do not carry any *EGFR* alteration [5].

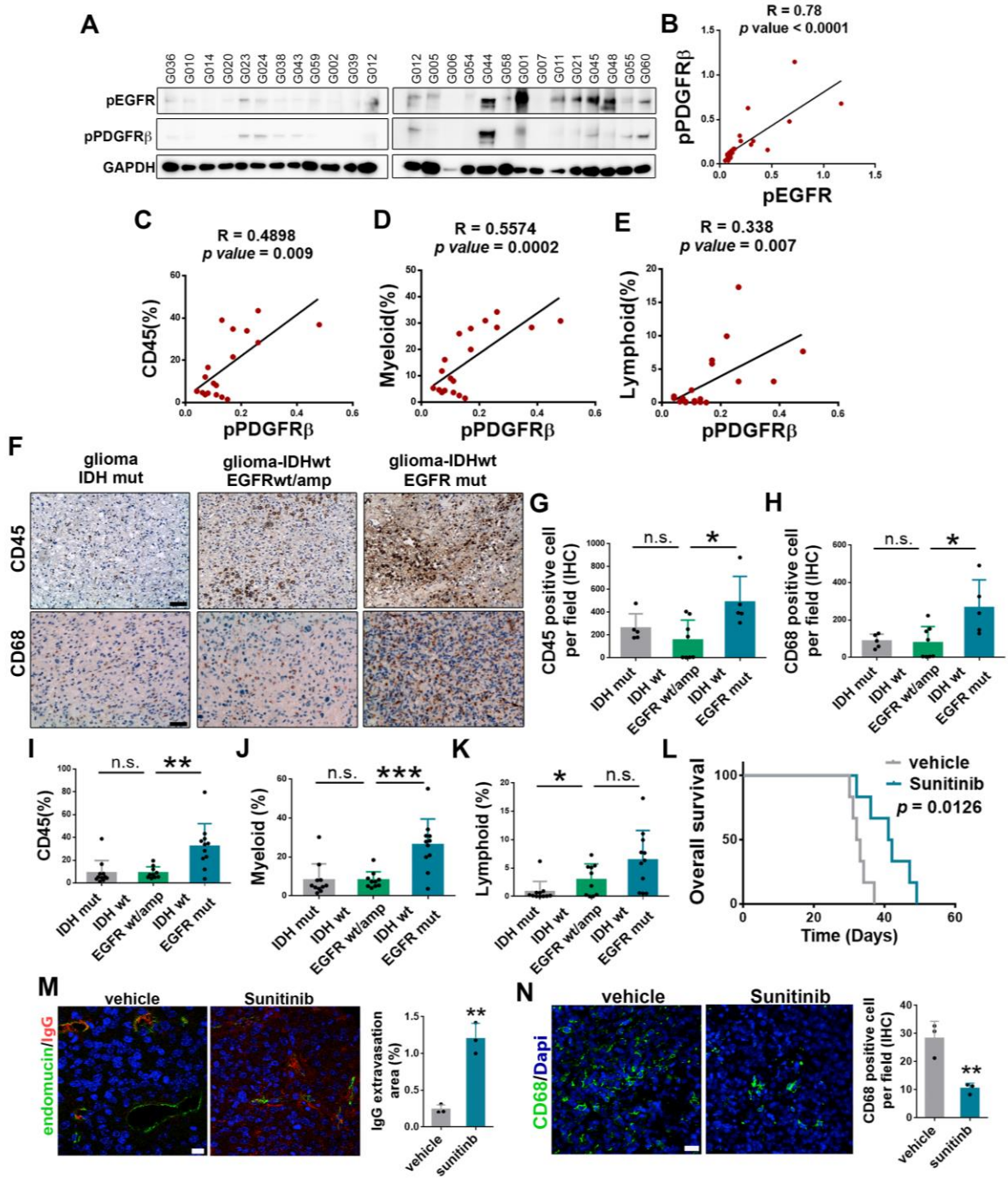

Fig 7. PDGFRβ activation in the pericytes of EGFR mutant gliomas is responsible for the entrance of immune cells into the tumors (A) WB analysis and quantification of pEGFR, pPDGFRβ in human tumors. GAPDH was used for normalization. **(B)** Correlation between pEGFR and pPDGFRβ in (A). **(C-E)** Correlation between the percentage of leukocytes (C),

myeloid cells (D) and lymphocytes (E) in dissociated human samples (flow cytometry analyses) and the levels of phospho-EGFR (WB analyses) in the same tumors. **(F)** Representative pictures of the IHC staining of CD45 (Top) and CD68 (Bottom) in samples from IDHmut, IDHwt/EGFRwt/amp and IDHwt/EGFRmut gliomas. **(G-H)** Quantification of the amount of CD45 (G) and CD68 (H) positive cells per field in the three groups of gliomas. (**I-K**) Percentage of leukocytes (I), myeloid cells (J) and lymphocytes (K) in the three groups of gliomas **(L)** Kaplan-Meier overall survival curves of mice that were orthotopically injected with SVZ-EGFRvIII cells and subsequently treated with intraperitoneal injection of sunitinib (6mg/kg/day) (n=6). **(M)** Representative images of endomucin and IgG IF staining in sections from tumors in (L). Quantification of IgG extravasation is shown on the right (n=3). **(N)** Representative images of CD68 IF staining in sections from tumors in (L). Quantification is shown on the right (n=3). *****P ≤ 0.05; **P ≤ 0.01; ***P ≤ 0.001; n.s. not significant. Scale bars: 10 μm (F), 25 μm (M).

The results presented so far indicates that the presence of EGFR mutations in gliomas lead to activation of PDGFRβ in the pericytes that cover the tumor vessels. Emerging evidence suggest that these mural cells are essential players in the regulation of blood cells extravasation [29]. Moreover, the activation of PDGFRβ in pericytes has been shown to promote a latent immunological phenotype, which results in the recruitment of large numbers of leukocytes into the brain [30]. In agreement with that, we found a strong positive correlation between the levels of phosphorylation of this receptor in human samples and the percentage of leukocytes (**Fig 7C**), myeloid (**Fig 7D**) and lymphoid (**Fig 7E**) cells detected by flow cytometry after tumor dissociation. The presence of these cells in gliomas also correlated with the levels of phospho-EGFR (**S7D-S7F Fig**). Altogether, these data suggest that tumors expressing EGFR mutations, through the modulation of the vessel wall, have a stronger immune infiltrate. Indeed, the IHC

analysis showed a significant accumulation of CD45 (leukocytes) (**Fig 7F and 7G**) and CD68 (myeloid cells) (**Fig 7F and 7H**) positive cells in IDHwt/EGFRmut tumors, compared to the other groups of gliomas. Besides, we detected increased amounts of leukocytes (**Fig 7I**), myeloid (**Fig 7J**) and lymphoid (**Fig 7K**) cells in these tumors when measured by flow cytometry.

In order to confirm the relevance of PDGFRβ activation in EGFRmut gliomas we exposed SVZ-EGFRvIII tumors to sunitinib, which reduced the amount of phosphorylated receptor in the tumors (**S7G Fig**). The drug impaired glioma growth and increased the overall survival of the injected mice (**Fig 7L**). In agreement with our previous results, we measured a reduced number of dilated BVs in the sunitinib-treated tumors (**S7H Fig**), concomitant with an increased IgG extravasation (**Fig 7M**) and an upregulation of the hypoxia-related signature (**S7J Fig**). In addition, sunitinib reduced the presence of immune cells in EGFRvIII tumors (**Fig 7N**). Altogether, these results confirm that the activation of PDGFRβ, upon recruitment of the pericytes to the vessels, is important for the permanence and the fully functional differentiation of these cells, stabilizing the vasculature in EGFRmut gliomas. Moreover, the data highlights that tumor-derived-pericytes drives tumor growth through the regulation of both, the vascular and the immune compartments of gliomas.

Discussion

In agreement with other authors [9, 31, 32], we have stablished a positive correlation between the presence of *EGFR* genetic alterations and the expression of angiogenic molecules and the appearance of vascular abnormalities. However, our data suggest for the first time that wild-type or mutant EGFR induce the formation of two distinct vascular phenotypes, which in turn differ from the normalized vasculature of mutant IDH1/2 gliomas. The first one is

characterized by the instability of the BBB and the induction of hypoxic signals and necrotic areas in the tumors, whereas the second phenotype, induced by EGFR mutations, contains more robust and enlarged tumor vessels that nurture a very compact and hyperproliferative tumor tissue. In agreement with this, the MRI analysis showed an accumulation of Gd over time in SVZ-EGFRwt/amp tumors. These results could seem contradictory with the literature as it has been suggested that EGFRvIII gliomas have a higher perfusion values in dynamic contrast-enhanced (DCE)-MRI analyses in the patients [33], as well as in animals models [34] [31]. This measure is related to the degree of vessel permeability, but it is also influenced by the blood flow and the vessel area, which are enlarged in SVZ-EGFRvIII compared to SVZ-EGFRwt/amp tumors. Based on our data, EGFRwt/amp tumors would show more contrast enhancement at longer times after Gd injection, due to the presence of leakier tumor vessels. Although long MRI studies are non-viable in clinical practice, emerging evidence indicates that multiparametric analysis of DCE-MRI data could offer greater insight into the status of the tumor vasculature [35]. Using such an approach, no major differences were described in the Gd enhancement of EGFRvIII gliomas, which were otherwise characterized by increased cell density and blood flow, compared to other tumors [36]. A similar study has revealed the existence of two different subtypes of IDHwt GBMs: a glycolytic phenotype with predominant neovasculature and a necrotic/hypoxic dominated phenotype. However, no correlation was stablished with the genetic status of *EGFR* [37]. These kind of studies or other approaches to measure tumor vessel caliber and/or structure in gliomas [15] would certainly help to characterize the contribution of the two different vascular ecosystems in IDHwt GBMs and how they evolve in response to therapy.

Pericytes play an essential role maintaining the structure and function of the vessel wall and the BBB. These mural cells were thought to originate from mesenchymal progenitors that are recruited from the bone-marrow in response to hypoxia [41, 42]. However, it has been

recently shown that the majority of vascular pericytes in GBMs derive from tumor cells [3]. A similar epithelial-to-pericyte transition has been proposed in other cancers, promoting vascular integrity and tumor growth [43]. Nevertheless, to date it was unknown if different genetic alterations could modulate this transdiferentation process. Results from this study and our recently published data [7] suggest that it is governed by the EGFR/BMX signaling pathway. Moreover, we have shown here that tumor cells expressing mutant isoforms of EGFR have a higher capacity to differentiate into functional pericytes and overexpress molecules such as CXCR4, CX45 and TIMP1, which could be responsible for the improved pericyte recruitment toward endothelial cells and the increase pericyte coverage observed in EGFRmut gliomas. These signals confer a higher aggressiveness to the tumors. However, they also increase their sensitivity to molecules that target pericytic function, such as ibrutinib. This BMX inhibitor specifically affects tumor-derived pericytes [27] and cancer stem cells [44], preserving normal brain cells, which could limit the toxicity of the drug. Besides, this compound inhibits mutant EGFR activity in gliomas [45], as well as in other cancers [46]. Ibrutinib is being tested on unselected GBM patients in combination with radio- and chemo-therapy (NCT03535350). We propose that its activity could be higher in tumors harboring EGFR mutations so future retrospective studies should be carried on to validate this idea.

Downstream of EGFRmut/BMX signaling, we have found an enrichment of *SOX9* expression and protein stability. The oncogenic function of SOX9 has been proposed in different cancers [26], including gliomas [47, 48], where it induces proliferation and cell survival, partly through BMI1 upregulation [49]. Our data indicate that SOX9 also regulates the vascular properties of gliomas by inducing the cellular plasticity of tumor cells, which could be linked to its well-known effects in cancer stem cells [26]. Notably, SOX9 has been linked to the upregulation of PDGFRα expression during development [50], and regulates genes involved in the extracellular matrix such as collagen, aggrecan and Timp1, which are involved

in the maintenance of the blood vessel structure [51]. In addition, BMI1 has been linked to the regulation of the epithelial-to-mesenchymal transition [52], allowing us to propose that SOX9, either acting directly or through the modulation of BMI1, may act as a master regulator of the vascularization processes in gliomas, especially for those tumors carrying *EGFR* mutations.

Our results suggest that once attached to the endothelial cells, there is an activation of PDGFRβ in the glioma-derived pericytes. This is a key signal for their fully differentiation and integration into the vessels, and provides the proliferative and survival cues needed to maintain the vascular structure [28]. Our results confirm the higher functionality of these tumor vessels in EGFR mutant tumors, as they are able to support the proliferative capacity of glioma cells and favor the extravasation of blood cells into the tumor stroma. Although pericytes were classically associated with structural functions, an accumulating body of evidence suggests that these cells also display immune properties, including antigen presenting activities and expression of cytokines and adhesion molecules to control the immune cell trafficking across vessel walls [29, 53]. Particularly, activation of PDGFRβ in pericytes has been shown to promote a latent immunological phenotype, which results in the expression of recruitment molecules in the adjacent endothelium and the entrance of large numbers of blood cells into the brain [30]. These results are in agreement with recent reports that strongly suggest that changes in the tumor vasculature affect the degree of extravasation of immune cells, as well as their pro or anti-tumor profiles [54-56]. Moreover, increasing evidences support the synergism between anti-angiogenic and immune-therapies in other cancers [57], as well as in gliomas [58]. Although no breakthrough has been achieved using sunitinib in GBM patients [59], our results suggest that there could be a synergistic effect with immune modulators. Moreover, we propose that patients harboring EGFR mutations could have a differential sensitivity, not only to PDGFRβ inhibitors but also to strategies targeting the immune compartment.

In the absence of EGFR mutations, we have found an induction of HIF1α protein and function. A direct transcriptional activation of *HIF1α* by EGFR has been proposed in lung cancer, especially in the presence of mutations [38], but little is known about this interaction in gliomas. Although we cannot discard a direct regulation of *HIF1α* expression by EGFR activation, we believe that this TF is induced and/or stabilized in the tumor context in response to the environmental conditions (such as acidosis or nutrients/oxygen deprivation) that occur after the disruption of the BBB in EGFRwt/amp gliomas. Notably, there seems to be a reciprocal relation as tumor hypoxia up-regulates *EGFR* expression in lung cancers [38], as well as in gliomas [39], promoting its activation in the absence of mutations. This could serve as a pro-survival signal for hypoxic cancer cells. Moreover, hypoxia has been proposed to induce resistance to EGFR inhibitors in different cancers [40], suggesting that combinatorial approaches targeting both pathways could be a promising strategy for EGFRwt/amp gliomas.

In summary, we propose the existence of two distinct microenvironmental phenotypes in IDHwt GBM, orchestrated by the genetic status of *EGFR* and the downstream modulation of BMX-SOX9 activity, which induces the transdifferentiation of tumor cells into pericytes (**Fig 8**). This model could have diagnostic as well as great predictive value, as the different subtypes could have a distinct sensitivity to anti-angiogenic or immunomodulatory strategies. Moreover, the function of the tumor-derived-pericytes could limit the entrance of cytotoxic therapies through the BBB [27, 60]. Overall, our results place the angiogenic properties of gliomas at the top of the glioma hierarchy and suggest that future combinatorial therapeutic approaches should combine agents targeting the glioma vasculature with conventional therapies, molecularly-directed drugs or immunotherapies. Moreover, these strategies should be tailor-designed for each specific glioma subtype.

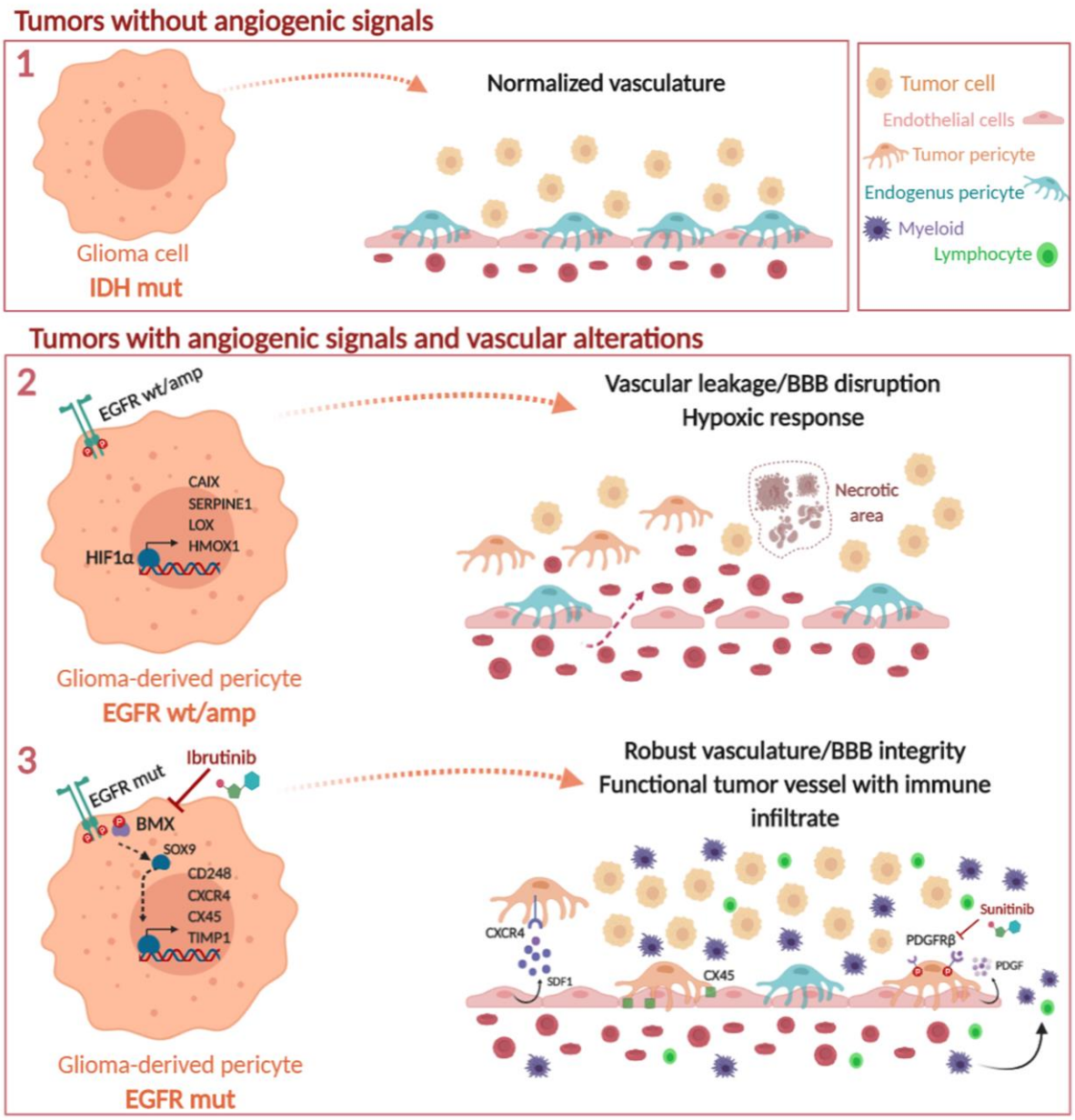

Fig 8. Schematic view of the role of IDH and EGFR on the regulation of the vascular structure and the immune infiltrate in the microenvironment of gliomas.

References

1. Louis DN, Perry A, Reifenberger G, von DA, Figarella-Branger D, Cavenee WK, et al. The 2016 World Health Organization Classification of Tumors of the Central Nervous System: a summary. Acta Neuropathol. 2016;131(6):803-20.
2. Hardee ME, Zagzag D. Mechanisms of glioma-associated neovascularization. AmJPathol. 2012;181(4):1126-41.
3. Cheng L, Huang Z, Zhou W, Wu Q, Donnola S, Liu JK, et al. Glioblastoma stem cells generate vascular pericytes to support vessel function and tumor growth. Cell. 2013;153(1):139-52.
4. Guerra DAP, Paiva AE, Sena IFG, Azevedo PO, Silva WN, Mintz A, et al. Targeting glioblastoma-derived pericytes improves chemotherapeutic outcome. Angiogenesis. 2018;21(4):667-75. Epub 2018/05/16. doi: 10.1007/s10456-018-9621-x. PubMed PMID: 29761249; PubMed Central PMCID: PMCPMC6238207.
5. Park JS, Kim IK, Han S, Park I, Kim C, Bae J, et al. Normalization of Tumor Vessels by Tie2 Activation and Ang2 Inhibition Enhances Drug Delivery and Produces a Favorable Tumor Microenvironment. Cancer Cell. 2016;30(6):953-67.
6. Conroy S, Wagemakers M, Walenkamp AM, Kruyt FA, Den Dunnen WF. Novel insights into vascularization patterns and angiogenic factors in glioblastoma subclasses. JNeurooncol. 2017;131(1):11-20.
7. Gargini R, Segura-Collar B, Herranz B, Garcia-Escudero V, Romero-Bravo A, Nunez FJ, et al. The IDH-TAU-EGFR triad defines the neovascular landscape of diffuse gliomas. SciTranslMed. 2020;12(527).
8. Zahonero C, Sanchez-Gomez P. EGFR-dependent mechanisms in glioblastoma: towards a better therapeutic strategy. Cell MolLife Sci. 2014.
9. Keller S, Schmidt MHH. EGFR and EGFRvIII Promote Angiogenesis and Cell Invasion in Glioblastoma: Combination Therapies for an Effective Treatment. IntJMolSci. 2017;18(6).
10. Ferron SR, Andreu-Agullo C, Mira H, Sanchez P, Marques-Torrejon MA, Farinas I. A combined ex/in vivo assay to detect effects of exogenously added factors in neural stem cells. NatProtoc. 2007;2(4):849-59.
11. Zahonero C, Aguilera P, Ramirez-Castillejo C, Pajares M, Bolos MV, Cantero D, et al. Preclinical test of dacomitinib, an irreversible EGFR inhibitor, confirms its effectiveness for glioblastoma. MolCancer Ther. 2015.
12. Casas BS, Vitória G, do Costa MN, Madeiro da Costa R, Trindade P, Maciel R, et al. hiPSC-derived neural stem cells from patients with schizophrenia induce an impaired angiogenesis. Transl Psychiatry. 2018;8(1):48. Epub 2018/02/23. doi: 10.1038/s41398-018-0095-9. PubMed PMID: 29467462; PubMed Central PMCID: PMCPMC5821759.
13. Cejalvo T, Gargini R, Segura-Collar B, Mata-Martínez P, Herranz B, Cantero D, et al. Immune profiling of gliomas reveals a connection with Tau function and the tumor vasculature. bioRxiv. 2020:2020.07.17.208165. doi: 10.1101/2020.07.17.208165.
14. Zhang L, He L, Lugano R, Roodakker K, Bergqvist M, Smits A, et al. IDH mutation status is associated with distinct vascular gene expression signatures in lower-grade gliomas. Neuro Oncol. 2018;20(11):1505-16. Epub 2018/05/31. doi: 10.1093/neuonc/noy088. PubMed PMID: 29846705; PubMed Central PMCID: PMCPMC6176806.
15. Emblem KE, Farrar CT, Gerstner ER, Batchelor TT, Borra RJ, Rosen BR, et al. Vessel caliber--a potential MRI biomarker of tumour response in clinical trials. Nat Rev Clin Oncol. 2014;11(10):566-84. Epub 2014/08/13. doi: 10.1038/nrclinonc.2014.126. PubMed PMID: 25113840; PubMed Central PMCID: PMCPMC4445139.
16. Edwards SS, Zavala G, Prieto CP, Elliott M, Martínez S, Egaña JT, et al. Functional analysis reveals angiogenic potential of human mesenchymal stem cells from Wharton's jelly in dermal regeneration. Angiogenesis. 2014;17(4):851-66. Epub 2014/04/15. doi: 10.1007/s10456-014-9432-7. PubMed PMID: 24728929.

17. Jain RK. Antiangiogenesis strategies revisited: from starving tumors to alleviating hypoxia. Cancer Cell. 2014;26(5):605-22. Epub 2014/12/18. doi: 10.1016/j.ccell.2014.10.006. PubMed PMID: 25517747; PubMed Central PMCID: PMCPMC4269830.
18. Verhaak RG, Hoadley KA, Purdom E, Wang V, Qi Y, Wilkerson MD, et al. Integrated genomic analysis identifies clinically relevant subtypes of glioblastoma characterized by abnormalities in PDGFRA, IDH1, EGFR, and NF1. Cancer Cell. 2010;17(1):98-110.
19. Mathew LK, Skuli N, Mucaj V, Lee SS, Zinn PO, Sathyan P, et al. miR-218 opposes a critical RTK-HIF pathway in mesenchymal glioblastoma. Proc Natl Acad Sci U S A. 2014;111(1):291-6. Epub 2013/12/26. doi: 10.1073/pnas.1314341111. PubMed PMID: 24368849; PubMed Central PMCID: PMCPMC3890843.
20. Phillips HS, Kharbanda S, Chen R, Forrest WF, Soriano RH, Wu TD, et al. Molecular subclasses of high-grade glioma predict prognosis, delineate a pattern of disease progression, and resemble stages in neurogenesis. Cancer Cell. 2006;9(3):157-73.
21. Lai A, Kharbanda S, Pope WB, Tran A, Solis OE, Peale F, et al. Evidence for sequenced molecular evolution of IDH1 mutant glioblastoma from a distinct cell of origin. JClinOncol. 2011;29(34):4482-90.
22. Simonavicius N, Robertson D, Bax DA, Jones C, Huijbers IJ, Isacke CM. Endosialin (CD248) is a marker of tumor-associated pericytes in high-grade glioma. ModPathol. 2008;21(3):308-15.
23. Gargini R, Segura-Collar B, Sanchez-Gomez P. Novel Functions of the Neurodegenerative-Related Gene Tau in Cancer. Front Aging Neurosci. 2019;11:231.
24. Liu F, Hon GC, Villa GR, Turner KM, Ikegami S, Yang H, et al. EGFR Mutation Promotes Glioblastoma through Epigenome and Transcription Factor Network Remodeling. MolCell. 2015;60(2):307-18.
25. Wang Z, Sun D, Chen YJ, Xie X, Shi Y, Tabar V, et al. Cell Lineage-Based Stratification for Glioblastoma. Cancer Cell. 2020. Epub 2020/07/11. doi: 10.1016/j.ccell.2020.06.003. PubMed PMID: 32649888.
26. Aguilar-Medina M, Avendaño-Félix M, Lizárraga-Verdugo E, Bermúdez M, Romero-Quintana JG, Ramos-Payan R, et al. SOX9 Stem-Cell Factor: Clinical and Functional Relevance in Cancer. J Oncol. 2019;2019:6754040. Epub 2019/05/07. doi: 10.1155/2019/6754040. PubMed PMID: 31057614; PubMed Central PMCID: PMCPMC6463569.
27. Zhou W, Chen C, Shi Y, Wu Q, Gimple RC, Fang X, et al. Targeting Glioma Stem Cell-Derived Pericytes Disrupts the Blood-Tumor Barrier and Improves Chemotherapeutic Efficacy. Cell Stem Cell. 2017;21(5):591-603.
28. Abramsson A, Lindblom P, Betsholtz C. Endothelial and nonendothelial sources of PDGF-B regulate pericyte recruitment and influence vascular pattern formation in tumors. JClinInvest. 2003;112(8):1142-51.
29. Rudziak P, Ellis CG, Kowalewska PM. Role and Molecular Mechanisms of Pericytes in Regulation of Leukocyte Diapedesis in Inflamed Tissues. Mediators Inflamm. 2019;2019:4123605. Epub 2019/06/18. doi: 10.1155/2019/4123605. PubMed PMID: 31205449; PubMed Central PMCID: PMCPMC6530229.
30. Olson LE, Soriano P. PDGFRβ signaling regulates mural cell plasticity and inhibits fat development. Dev Cell. 2011;20(6):815-26. Epub 2011/06/15. doi: 10.1016/j.devcel.2011.04.019. PubMed PMID: 21664579; PubMed Central PMCID: PMCPMC3121186.
31. Eskilsson E, Rosland GV, Talasila KM, Knappskog S, Keunen O, Sottoriva A, et al. EGFRvIII mutations can emerge as late and heterogenous events in glioblastoma development and promote angiogenesis through Src activation. Neuro Oncol. 2016;18(12):1644-55. Epub 2016/06/12. doi: 10.1093/neuonc/now113. PubMed PMID: 27286795; PubMed Central PMCID: PMCPMC5791772.
32. Katanasaka Y, Kodera Y, Kitamura Y, Morimoto T, Tamura T, Koizumi F. Epidermal growth factor receptor variant type III markedly accelerates angiogenesis and tumor growth via inducing c-myc mediated angiopoietin-like 4 expression in malignant glioma. Molecular Cancer. 2013;12(1):31. doi: 10.1186/1476-4598-12-31.

33. Arevalo-Perez J, Thomas AA, Kaley T, Lyo J, Peck KK, Holodny AI, et al. T1-Weighted Dynamic Contrast-Enhanced MRI as a Noninvasive Biomarker of Epidermal Growth Factor Receptor vIII Status. AJNR Am J Neuroradiol. 2015;36(12):2256-61. Epub 2015/09/05. doi: 10.3174/ajnr.A4484. PubMed PMID: 26338913; PubMed Central PMCID: PMCPMC4724408.
34. Politi LS, Brugnara G, Castellano A, Cadioli M, Altabella L, Peviani M, et al. T1-Weighted Dynamic Contrast-Enhanced MRI Is a Noninvasive Marker of Epidermal Growth Factor Receptor vIII Status in Cancer Stem Cell-Derived Experimental Glioblastomas. AJNR Am J Neuroradiol. 37. United States2016. p. E49-51.
35. O'Connor JP, Jackson A, Parker GJ, Roberts C, Jayson GC. Dynamic contrast-enhanced MRI in clinical trials of antivascular therapies. Nat Rev Clin Oncol. 2012;9(3):167-77. Epub 2012/02/15. doi: 10.1038/nrclinonc.2012.2. PubMed PMID: 22330689.
36. Akbari H, Bakas S, Pisapia JM, Nasrallah MP, Rozycki M, Martinez-Lage M, et al. In vivo evaluation of EGFRvIII mutation in primary glioblastoma patients via complex multiparametric MRI signature. Neuro Oncol. 2018;20(8):1068-79. Epub 2018/04/05. doi: 10.1093/neuonc/noy033. PubMed PMID: 29617843; PubMed Central PMCID: PMCPMC6280148.
37. Stadlbauer A, Zimmermann M, Doerfler A, Oberndorfer S, Buchfelder M, Coras R, et al. Intratumoral heterogeneity of oxygen metabolism and neovascularization uncovers 2 survival-relevant subgroups of IDH1 wild-type glioblastoma. Neuro Oncol. 2018;20(11):1536-46. Epub 2018/05/03. doi: 10.1093/neuonc/noy066. PubMed PMID: 29718366; PubMed Central PMCID: PMCPMC6176796.
38. Swinson DE, O'Byrne KJ. Interactions between hypoxia and epidermal growth factor receptor in non-small-cell lung cancer. Clin Lung Cancer. 2006;7(4):250-6. Epub 2006/03/04. doi: 10.3816/CLC.2006.n.002. PubMed PMID: 16512978.
39. Franovic A, Gunaratnam L, Smith K, Robert I, Patten D, Lee S. Translational up-regulation of the EGFR by tumor hypoxia provides a nonmutational explanation for its overexpression in human cancer. Proc Natl Acad Sci U S A. 2007;104(32):13092-7. Epub 2007/08/03. doi: 10.1073/pnas.0702387104. PubMed PMID: 17670948; PubMed Central PMCID: PMCPMC1941796.
40. Wouters A, Boeckx C, Vermorken JB, Van den Weyngaert D, Peeters M, Lardon F. The intriguing interplay between therapies targeting the epidermal growth factor receptor, the hypoxic microenvironment and hypoxia-inducible factors. Curr Pharm Des. 2013;19(5):907-17. Epub 2012/09/15. PubMed PMID: 22973959.
41. De Palma M, Venneri MA, Galli R, Sergi Sergi L, Politi LS, Sampaolesi M, et al. Tie2 identifies a hematopoietic lineage of proangiogenic monocytes required for tumor vessel formation and a mesenchymal population of pericyte progenitors. Cancer Cell. 2005;8(3):211-26. Epub 2005/09/20. doi: 10.1016/j.ccr.2005.08.002. PubMed PMID: 16169466.
42. Du R, Lu KV, Petritsch C, Liu P, Ganss R, Passegue E, et al. HIF1alpha induces the recruitment of bone marrow-derived vascular modulatory cells to regulate tumor angiogenesis and invasion. Cancer Cell. 2008;13(3):206-20.
43. Shenoy AK, Jin Y, Luo H, Tang M, Pampo C, Shao R, et al. Epithelial-to-mesenchymal transition confers pericyte properties on cancer cells. JClinInvest. 2016;126(11):4174-86.
44. Shi Y, Guryanova OA, Zhou W, Liu C, Huang Z, Fang X, et al. Ibrutinib inactivates BMX-STAT3 in glioma stem cells to impair malignant growth and radioresistance. Sci Transl Med. 2018;10(443). Epub 2018/06/01. doi: 10.1126/scitranslmed.aah6816. PubMed PMID: 29848664; PubMed Central PMCID: PMCPMC6431250.
45. Lee JK, Liu Z, Sa JK, Shin S, Wang J, Bordyuh M, et al. Pharmacogenomic landscape of patient-derived tumor cells informs precision oncology therapy. Nat Genet. 2018;50(10):1399-411. Epub 2018/09/29. doi: 10.1038/s41588-018-0209-6. PubMed PMID: 30262818.
46. Gao W, Wang M, Wang L, Lu H, Wu S, Dai B, et al. Selective antitumor activity of ibrutinib in EGFR-mutant non-small cell lung cancer cells. Journal of the National Cancer Institute. 2014;106(9):dju204. doi: 10.1093/jnci/dju204. PubMed PMID: 25214559.

47. Wang L, He S, Yuan J, Mao X, Cao Y, Zong J, et al. Oncogenic role of SOX9 expression in human malignant glioma. Med Oncol. 2012;29(5):3484-90. Epub 2012/06/21. doi: 10.1007/s12032-012-0267-z. PubMed PMID: 22714060.
48. Garros-Regulez L, Aldaz P, Arrizabalaga O, Moncho-Amor V, Carrasco-Garcia E, Manterola L, et al. mTOR inhibition decreases SOX2-SOX9 mediated glioma stem cell activity and temozolomide resistance. Expert Opin Ther Targets. 2016;20(4):393-405. Epub 2016/02/16. doi: 10.1517/14728222.2016.1151002. PubMed PMID: 26878385; PubMed Central PMCID: PMCPMC4898154.
49. Aldaz P, Otaegi-Ugartemendia M, Saenz-Antoñanzas A, Garcia-Puga M, Moreno-Valladares M, Flores JM, et al. SOX9 promotes tumor progression through the axis BMI1-p21(CIP). Sci Rep. 2020;10(1):357. Epub 2020/01/17. doi: 10.1038/s41598-019-57047-w. PubMed PMID: 31941916; PubMed Central PMCID: PMCPMC6962164.
50. Finzsch M, Stolt CC, Lommes P, Wegner M. Sox9 and Sox10 influence survival and migration of oligodendrocyte precursors in the spinal cord by regulating PDGF receptor alpha expression. Development. 2008;135(4):637-46. Epub 2008/01/11. doi: 10.1242/dev.010454. PubMed PMID: 18184726.
51. Lafont JE, Talma S, Hopfgarten C, Murphy CL. Hypoxia promotes the differentiated human articular chondrocyte phenotype through SOX9-dependent and -independent pathways. J Biol Chem. 2008;283(8):4778-86. Epub 2007/12/14. doi: 10.1074/jbc.M707729200. PubMed PMID: 18077449.
52. Jin X, Kim LJY, Wu Q, Wallace LC, Prager BC, Sanvoranart T, et al. Targeting glioma stem cells through combined BMI1 and EZH2 inhibition. Nat Med. 2017;23(11):1352-61. Epub 2017/10/17. doi: 10.1038/nm.4415. PubMed PMID: 29035367; PubMed Central PMCID: PMCPMC5679732.
53. Navarro R, Compte M, Álvarez-Vallina L, Sanz L. Immune Regulation by Pericytes: Modulating Innate and Adaptive Immunity. Front Immunol. 2016;7:480. Epub 2016/11/22. doi: 10.3389/fimmu.2016.00480. PubMed PMID: 27867386; PubMed Central PMCID: PMCPMC5095456.
54. Kloepper J, Riedemann L, Amoozgar Z, Seano G, Susek K, Yu V, et al. Ang-2/VEGF bispecific antibody reprograms macrophages and resident microglia to anti-tumor phenotype and prolongs glioblastoma survival. ProcNatlAcadSciUSA. 2016;113(16):4476-81.
55. Turkowski K, Brandenburg S, Mueller A, Kremenetskaia I, Bungert AD, Blank A, et al. VEGF as a modulator of the innate immune response in glioblastoma. Glia. 2018;66(1):161-74.
56. Sidibe A, Ropraz P, Jemelin S, Emre Y, Poittevin M, Pocard M, et al. Angiogenic factor-driven inflammation promotes extravasation of human proangiogenic monocytes to tumours. NatCommun. 2018;9(1):355.
57. Schmittnaegel M, Rigamonti N, Kadioglu E, Cassara A, Wyser Rmili C, Kiialainen A, et al. Dual angiopoietin-2 and VEGFA inhibition elicits antitumor immunity that is enhanced by PD-1 checkpoint blockade. Science translational medicine. 2017;9(385). Epub 2017/04/14. doi: 10.1126/scitranslmed.aak9670. PubMed PMID: 28404865.
58. He B, Jabouille A, Steri V, Johansson-Percival A, Michael IP, Kotamraju VR, et al. Vascular targeting of LIGHT normalizes blood vessels in primary brain cancer and induces intratumoural high endothelial venules. JPathol. 2018;245(2):209-21.
59. Kreisl TN, Smith P, Sul J, Salgado C, Iwamoto FM, Shih JH, et al. Continuous daily sunitinib for recurrent glioblastoma. J Neurooncol. 2013;111(1):41-8. Epub 2012/10/23. doi: 10.1007/s11060-012-0988-z. PubMed PMID: 23086433.
60. Arvanitis CD, Ferraro GB, Jain RK. The blood-brain barrier and blood-tumour barrier in brain tumours and metastases. Nat Rev Cancer. 2020;20(1):26-41. Epub 2019/10/12. doi: 10.1038/s41568-019-0205-x. PubMed PMID: 31601988.

Acknowledgments: We would like to acknowledge Manuel Serrano for kindly donating the p16/p19 ko mice and Jacqueline Gutiérrez and Rafael Hortigüela for their technical support. Figure 8 was created with BioRender.

Funding: Work was supported by FONDECYT grant (1140697) to VP, CONICYT Fellowship to BSC, by Ministerio de Economía y Competitividad and FEDER funds: PI13/01258 to AHL, PI16/01278 to JMS, and PI16/01580 and DTS18/00181 to AM, by Young Employment Initiative (Comunidad de Madrid) to MG, by "Asociación Española contra el Cancer (AECC) grants: INVES192GARG to RG and GCTRA16015SEDA to JMS; and by Ministerio de Ciencia, Innovación y Universidades and FEDER funds (RTI2018-093596) to PSG.

Author contributions: Conceptualization: RG, BSC, and PSG; Investigation: RG, BSC, MGA, BH, EHS, TC and BC; Formal Analysis: BSC and RG; Resources: VP, AM, APN, JMS and AHL; Writing-Original Draft: RG, BSC and PSG; Writing-Review & Editing: MGA, BH, EHS, VP and AM; Funding Acquisition: RG, JMS and PSG; Supervision: RG and PSG.

Competing interests: The authors declare that they have no competing interests.

Data and materials availability: All data associated with this study are present in the paper or the Supplementary Materials.

List of Supplementary Materials

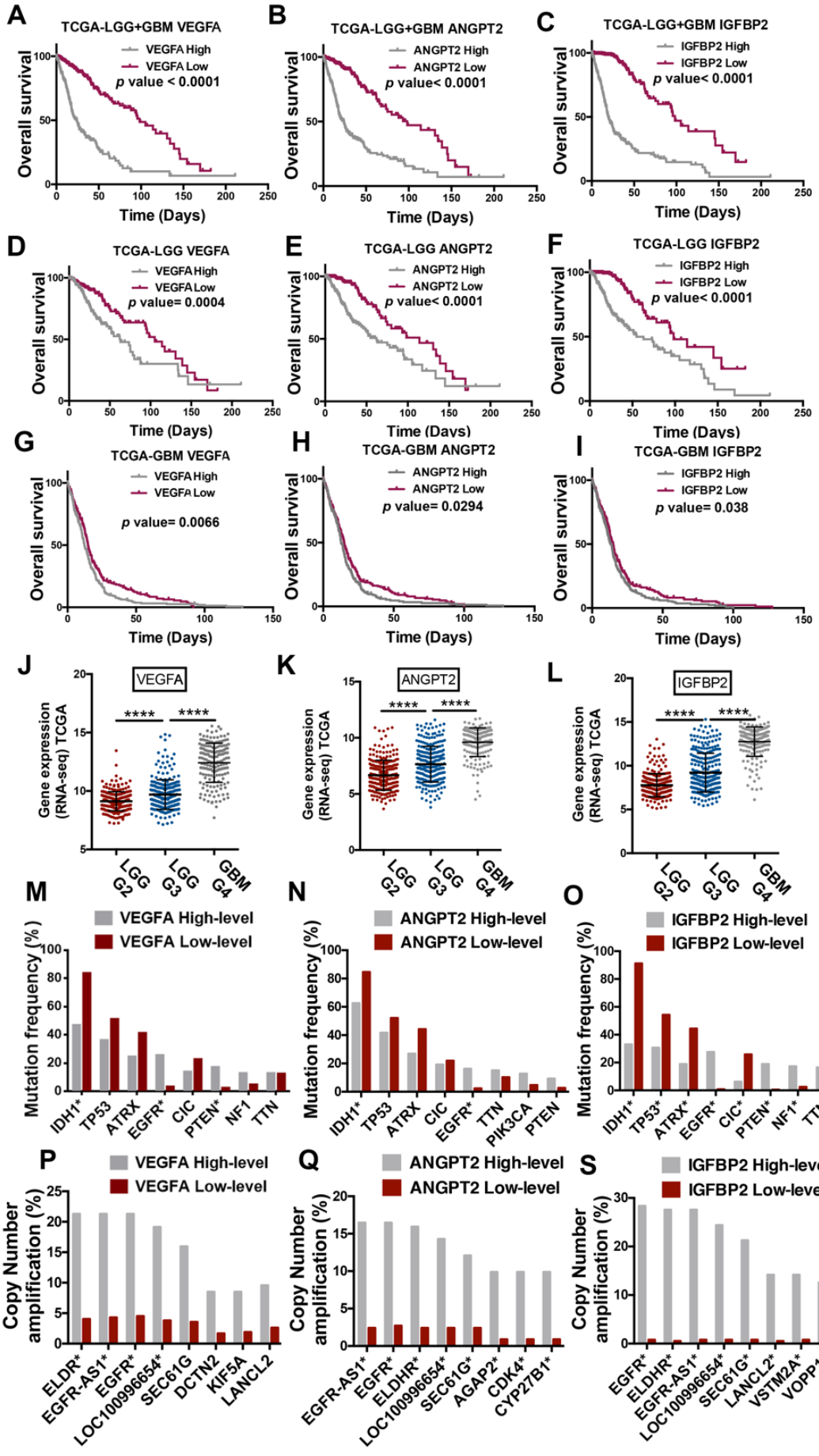
A
TCGA-LGG+GBM VEGFA
VEGFA High
VEGFA Low
p value < 0.0001
Overall survival
Time (Days)
B
TCGA-LGG+GBM ANGPT2
ANGPT2 High
ANGPT2 Low
p value< 0.0001
C
TCGA-LGG+GBM IGFBP2
IGFBP2 High
IGFBP2 Low
p value< 0.0001
D
TCGA-LGG VEGFA
p value= 0.0004
E
TCGA-LGG ANGPT2
p value< 0.0001
F
TCGA-LGG IGFBP2
p value< 0.0001
G
TCGA-GBM VEGFA
p value= 0.0066
H
TCGA-GBM ANGPT2
p value= 0.0294
I
TCGA-GBM IGFBP2
p value= 0.038
J
VEGFA
Gene expression (RNA-seq) TCGA
****
LGG G2
LGG G3
GBM G4
K
ANGPT2
L
IGFBP2
M
VEGFA High-level
VEGFA Low-level
Mutation frequency (%)
IDH1* TP53 ATRX EGFR* CIC PTEN* NF1 TTN
N
ANGPT2 High-level
ANGPT2 Low-level
IDH1* TP53 ATRX CIC EGFR* TTN PIK3CA PTEN
O
IGFBP2 High-level
IGFBP2 Low-level
IDH1* TP53* ATRX* EGFR* CIC* PTEN* NF1* TTN
P
VEGFA High-level
VEGFA Low-level
Copy Number amplification (%)
ELDR* EGFR-AS1* EGFR* LOC100996654* SEC61G DCTN2 KIF5A LANCL2
Q
ANGPT2 High-level
ANGPT2 Low-level
EGFR-AS1* EGFR* ELDHR* LOC100996654* SEC61G* AGAP2* CDK4* CYP27B1*
S
IGFBP2 High-level
IGFBP2 Low-level
EGFR* ELDHR* EGFR-AS1* LOC100996654* SEC61G* LANCL2* VSTM2A* VOPP1*

Supplementary Fig. 1. Association between the levels of angiogenic molecules and the aggressiveness and the genetic alterations of gliomas. (A-C) Kaplan-Meier overall survival curves of patients from the TCGA-LGG cohort (n=507). Patients were stratified into two groups based on high and low *VEGFA* (A), *ANGPT2* (B) or *IGFBP2* (C) expression values. **(D-F)** Kaplan-Meier overall survival curves of patients from the TCGA-GBM cohort (n=525). Patients were stratified into two groups based on high and low *VEGFA* (D), *ANGPT2* (E) or *IGFBP2* (F) expression values. **(G-I)** Kaplan-Meier overall survival curves of patients (TCGA, LGG+GBM cohort) (n=663), stratified into two groups based on high and low *VEGFA* (G), *ANGPT2* (H) or *IGFBP2* (I) expression values. **(J-L)** Analysis of *VEGFA* (J), *ANGPT2* (K) and *IGFBP2* (L) expression by RNAseq in gliomas (TCGA, LGG+GBM cohort) (n=663), grouped according to the clinical evolution (grade) of the tumors. **(M-S)** Frequency of gene mutations (M-O) or copy number amplification (P-S) in gliomas with high or low level of expression of *VEGFA* (M, P), *ANGPT2* (N, Q) and *IGFBP2* (O, S) (n=661). *P ≤ 0.05, ****P ≤ 0.0001.

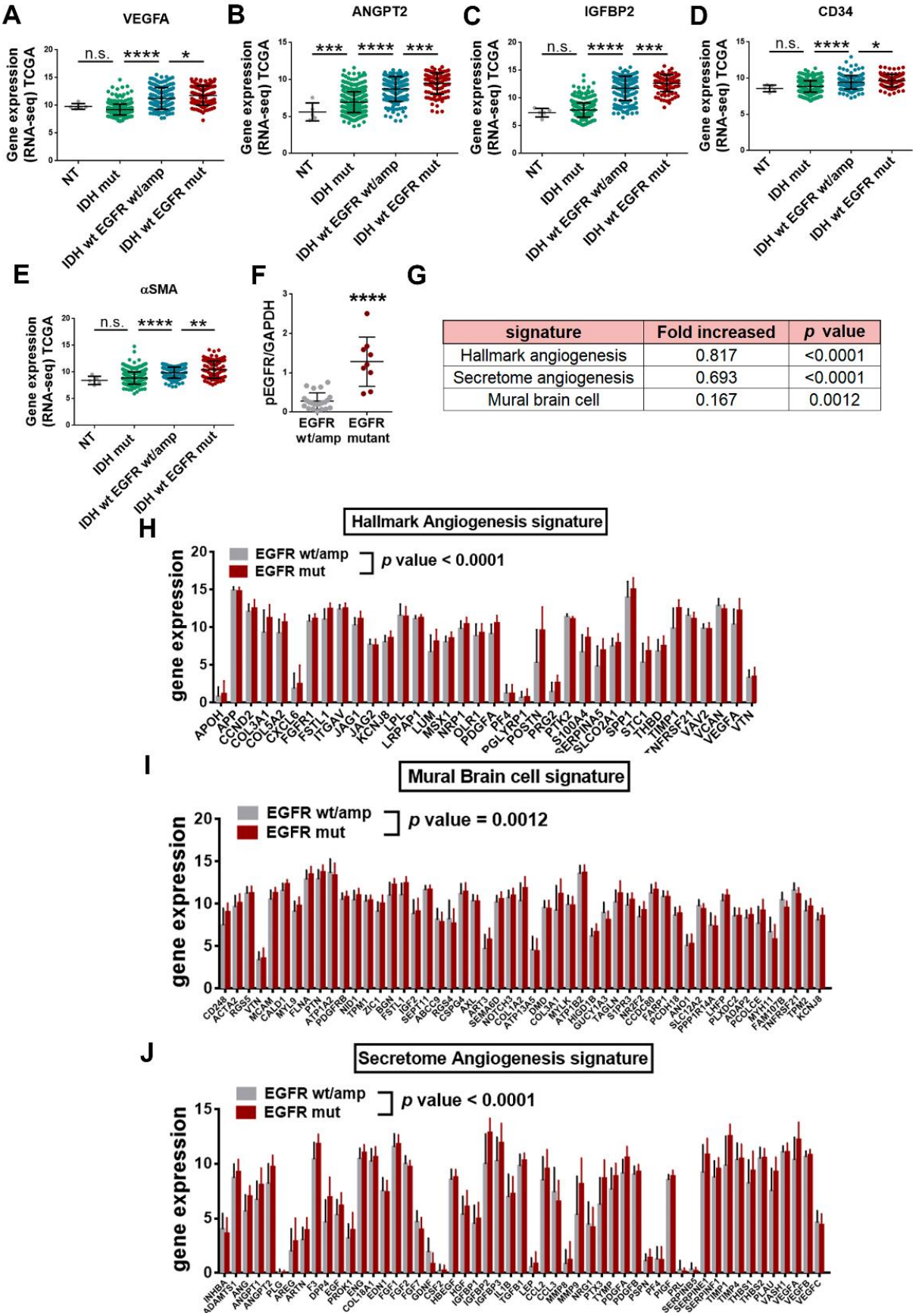

Supplementary Fig. 2. Analysis of *EGFR-IDH* alterations and vascular molecules in human samples. (A-E) Analysis of mRNA levels of *VEGFA* (A), *ANGPT2* (B), *IGFBP2* (C),

CD34 (D) and *αSMA* (E) (RNAseq) in gliomas from the TCGA (LGG+GBM) cohort (n= 661). Tumors were stratified in three groups: IDHmut, IDHwt/EGFRwt/amp and IDHwt/GFRmut. **(F)** Quantification of the WB analysis of pEGFR in patients stratified in two groups based on *EGFR* alterations (n=33). **(G)** Summary of the expression of genes from each signature showed below (H-J). The table depicts the fold increase expression in EGFRmut compared to EGFRwt/amp tumors and the p value of the increment in the expression. **(H-J)** Levels of expression of different signatures: hallmark angiogenesis (H), mural brain cell (I) and angiogenic secretome (J), in wt/amp or mut EGFR gliomas from the TCGA (LGG+GBM) cohort (n=319). *P ≤ 0.05; **P ≤ 0.01; ***P ≤ 0.001 ****P ≤ 0.0001; n.s. not significant.

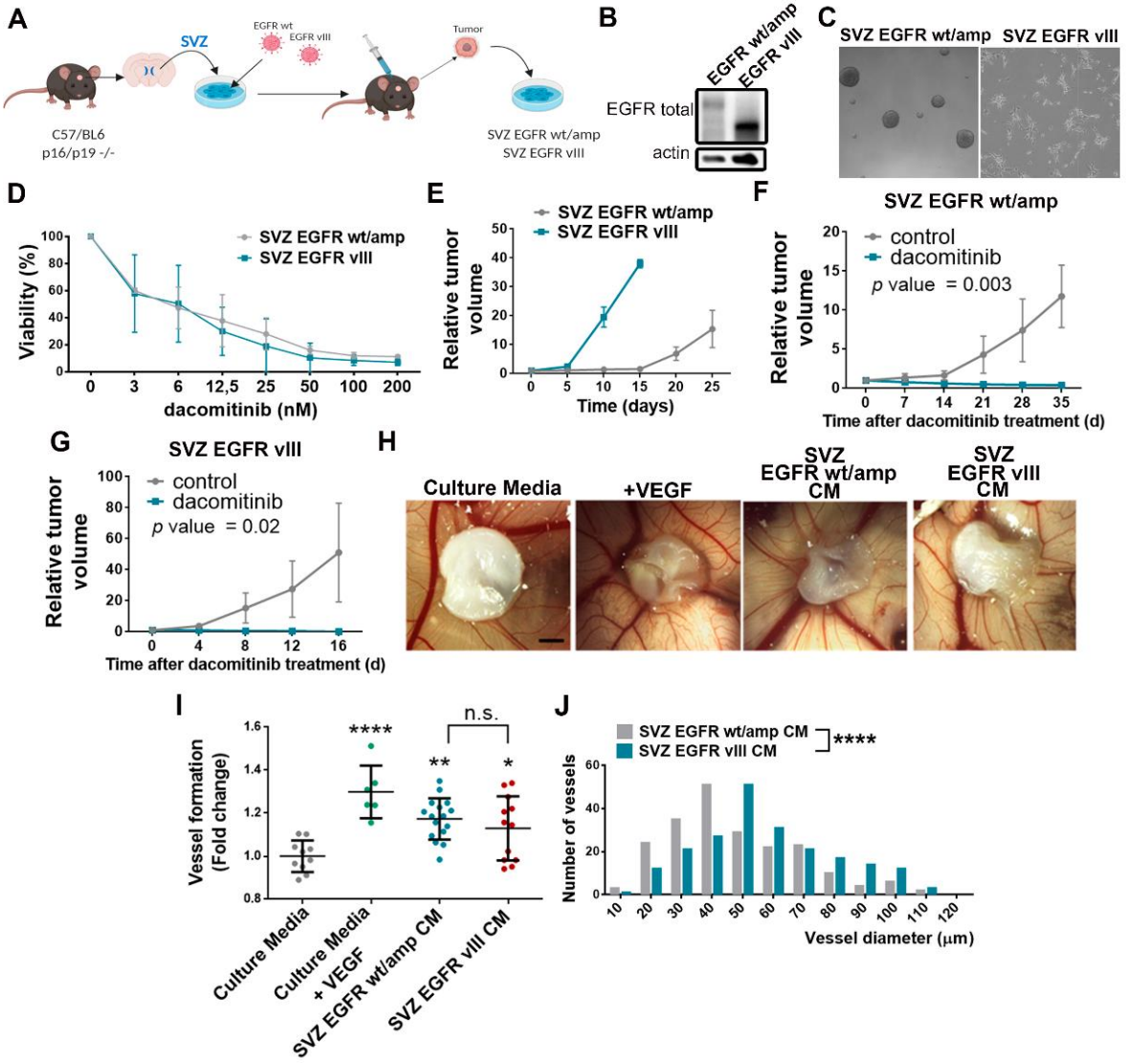

Supplementary Fig. 3. Characterization of the murine glioma models: SVZ EGFR wt/amp and SVZ EGFR vIII. (A) Representative diagram of the generation of the SVZ-EGFRwt/amp and the SVZ-EGFRvIII murine glioma models. **(B)** WB analysis of total EGFR in SVZ cell lines. Actin expression was used for normalization. **(C)** Representative images of SVZ cell lines grown *in vitro*. **(D)** Viability (represented as percentage related to the control) of SVZ cell lines grown *in vitro* in the presence of different concentrations of dacomitinib. **(E)** SVZ-EGFRwt/amp and SVZ-EGFRvIII were implanted subcutaneously in the nude mice and tumor growth was measured with a caliper. The graph represents the fold increase in tumor volume (n=3). **(F-G)** SVZ-EGFRwt/amp (F) and SVZ-EGFRvIII (G) cells were implanted subcutaneously in the nude mice. When tumors became visible, animals were treated with dacomitinib (15mg/Kg/day). The graphs represent the fold increase in tumor volume (n=5). **(H)** Representative images of blood vessel formation around the bio-cellulose scaffolds. Scaffolds were incubated with culture media, culture media with VEGF (as a positive control) and culture media with conditioned media (CM) from SVZ-EGFRwt/amp or SVZ-EGFRvIII cells. **(I-J)** Analysis of the number of vessels (I) and the vessel diameter (J) in each condition in (H). ****P $\leq$ 0.0001, n.s. not significant. Scale bar: 100 μm.

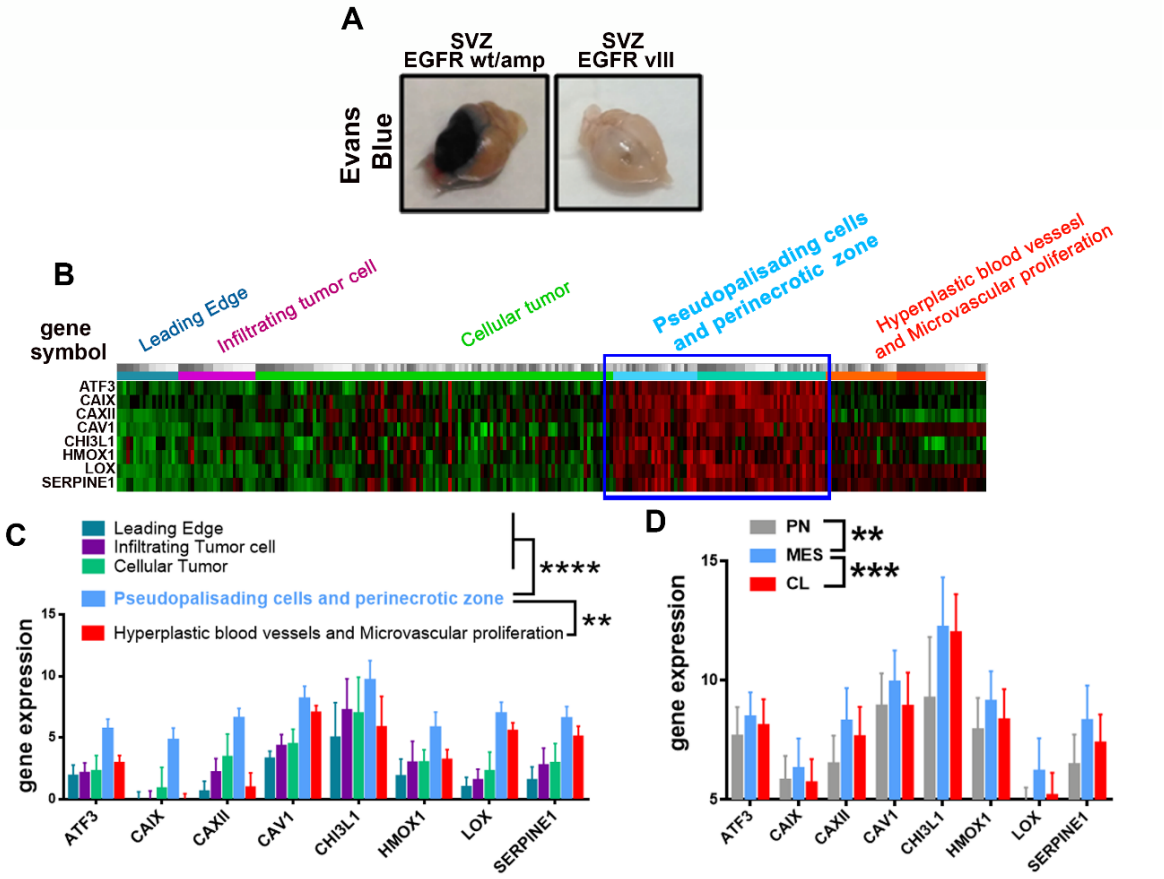

Supplementary Fig. 4. Association of EGFR alterations with BBB leakage and definition of a hypoxia signature in gliomas. (A) Representative image of the whole brain of mice harboring SVZ-EGFRwt/amp or SVZ-EGFRvIII gliomas tumor showing Evans Blue extravasation. **(B)** Selection of the most relevant genes of the hypoxia and the HIF1α pathway signatures that were up-regulated in the perinecreotic and pseudopalisading cell necrosis zones. YvyGap (IVY Glioblastoma atlas project) data set analysis was used. **(C)** Levels of expression of the hypoxic-related signature in gliomas of the TCGA (GBM) cohorts depending on the different anatomical regions of the tumors. **(D)** Levels of expression of the hypoxic-related signature in gliomas of the TCGA (GBM) cohort according to the molecular subtype's classification. PN: proneural, MES: mesenchymal, CL: classic. **P ≤ 0.01; ***P ≤ 0.001: ****P ≤ 0.0001

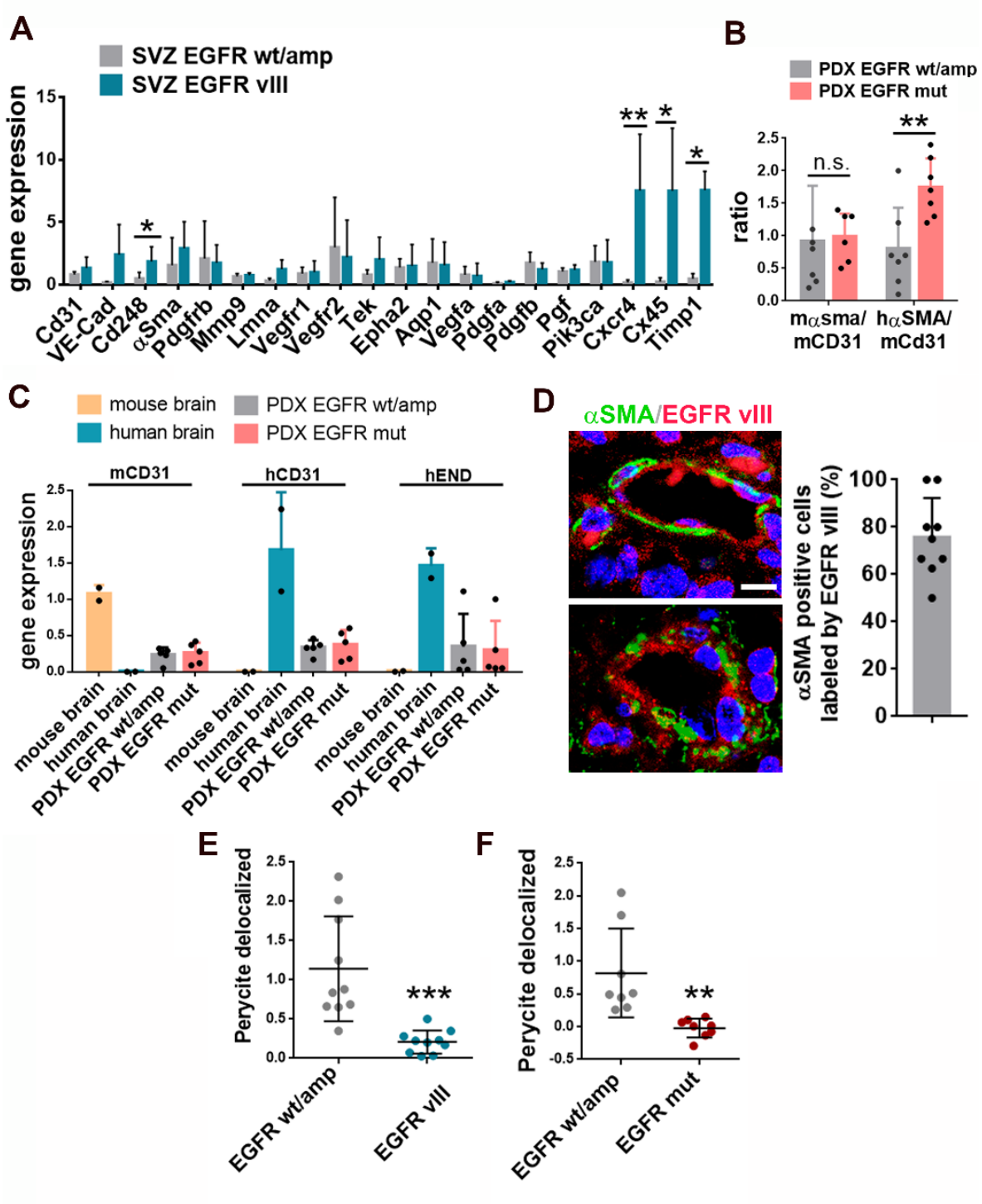

Supplementary Fig. 5. Participation of EGFR mutations in the formation of glioma-derived pericytes. (A) qRT-PCR analysis of angiogenesis-related genes in SVZ-EGFRwt/amp and SVZ-EGFRvIII cells. *Actin* was used for normalization (n=3). **(B)** Ratio of the expression of pericyte (mouse and human) to endothelial (mouse) genes (qRT-PCR analysis) in PDXs models expressing wt/amp or mut EGFR (n=7). **(C)** qRT-PCR analysis of endothelial–related

genes in EGFRwt/amp and EGFRmut tumor xenografts. Human or mouse tissue was used as control. *HPRT* or A*ctin* was used for normalization (n=5). **(D)** Representative images of αSMA and EGFRvIII immunofluorescent (IF) staining of sections from a tumor sample expressing EGFRvIII. The graph on the right shows the quantification of the fraction of pericytes carrying the EGFRvIII genetic alteration per field (n=9). **(E-F)** Quantification of the number of delocalized pericytes delocated in SVZ (E) or PDX (F) tumor sections. *P ≤ 0.05; **P ≤ 0.01; ***P ≤ 0.001; n.s. not significant. Scale bar: 10 μm.

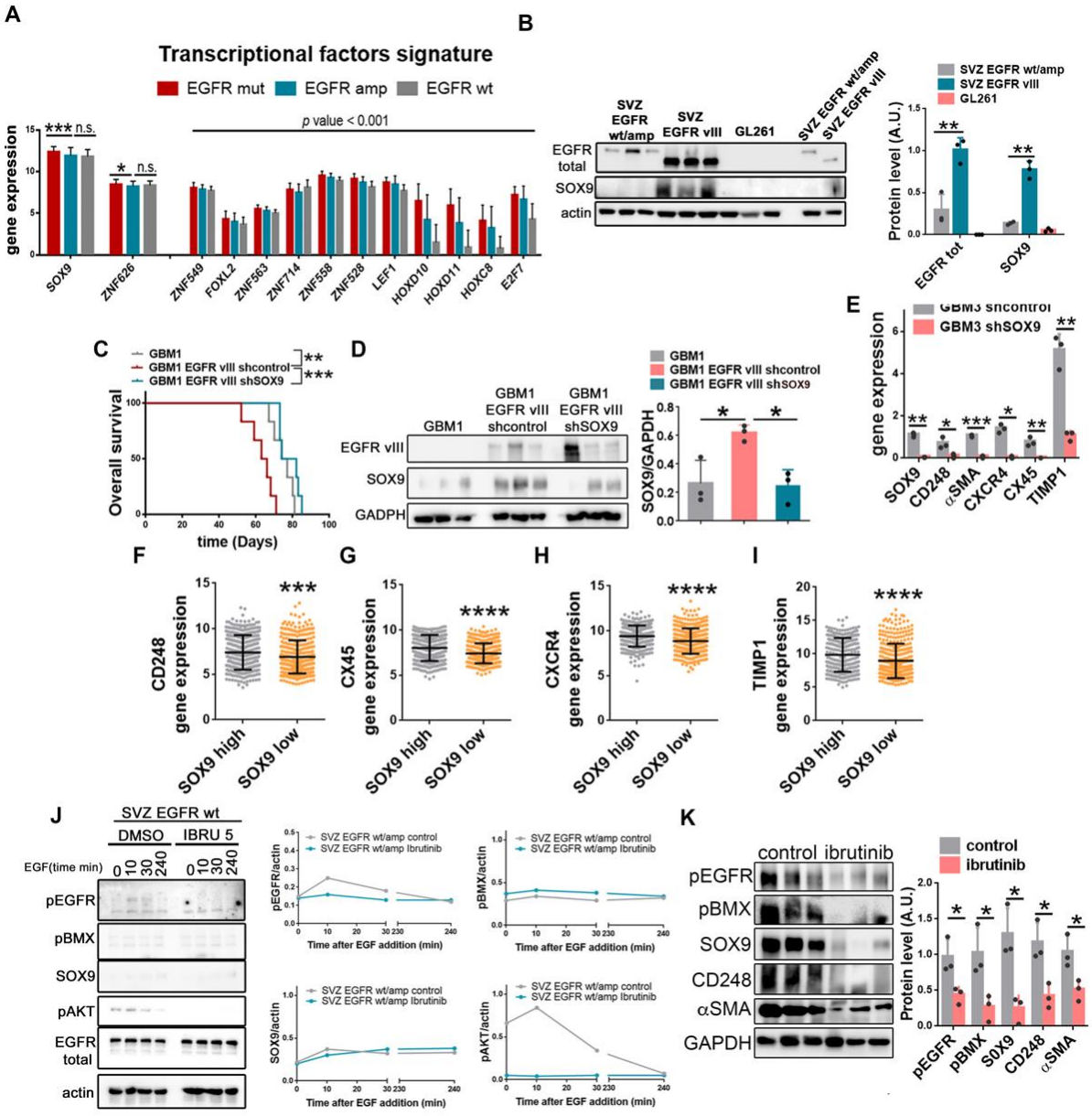

Supplementary Fig. 6. Correlation of SOX9 expression with EGFR mutations in gliomas. **(A)** Analysis of the expression of different transcription factors (RNAseq) in gliomas from the TCGA GBM+LGG cohort, n=306, grouped according to the genetic status of *EGFR*. **(B)** WB analysis and quantification of EGFR and SOX9 in tumor tissue extracts from SVZ and GL261 tumors. Extracts from SVZ cells were used as controls and loaded on the right. The expression of Actin was used for normalization **(C)** Kaplan-Meier overall survival curves of mice that were orthotopically injected with GBM1, GBM1-EGFRvIII and GBM1-EGFRvIII-shSOX9 (n=6)**.** **(D)** WB analysis of SOX9 expression in tumor tissue extracts from (C). GAPDH expression

was used for normalization (n=3). **(E)** qRT-PCR analysis of *SOX9*, *CD248*, *αSMA*, *CXCR4*, *CX45* and *TIMP1* in the tumors formed by GBM3-shControl or GBM3-shSOX9 cells. The expression of *HPRT* was used for normalization (n=3). **(F-I)** Analysis of *CD248* (F), *CX45* (G), *CXCR4* (H) and *TIMP1* (I) mRNA expression (RNAseq) in gliomas from the TCGA LGG+GBM cohort (n=702). Tumors were classified in two groups based on high or low SOX9 expression values. **(J)** WB analysis and quantification of pEGFR, pBMX, SOX9, pAKT and total EGFR total in extracts from SVZ-EGFRwt/amp cells incubated with EGF (100ng/ml) for the times indicated, in the presence of DMSO or Ibrutinib (5µm). Actin was used as loading control. **(K)** WB analysis and quantification of pEGFR, pBMX, SOX9, CD248 and αSMA in the tumors in SVZ-EGFRvIII tumors treated with control or ibrutinib (12mg/kg/day) (n=6). GAPDH was used for normalization. *P ≤ 0.05; **P ≤ 0.01; ***P ≤ 0.001; ****P ≤ 0.0001.

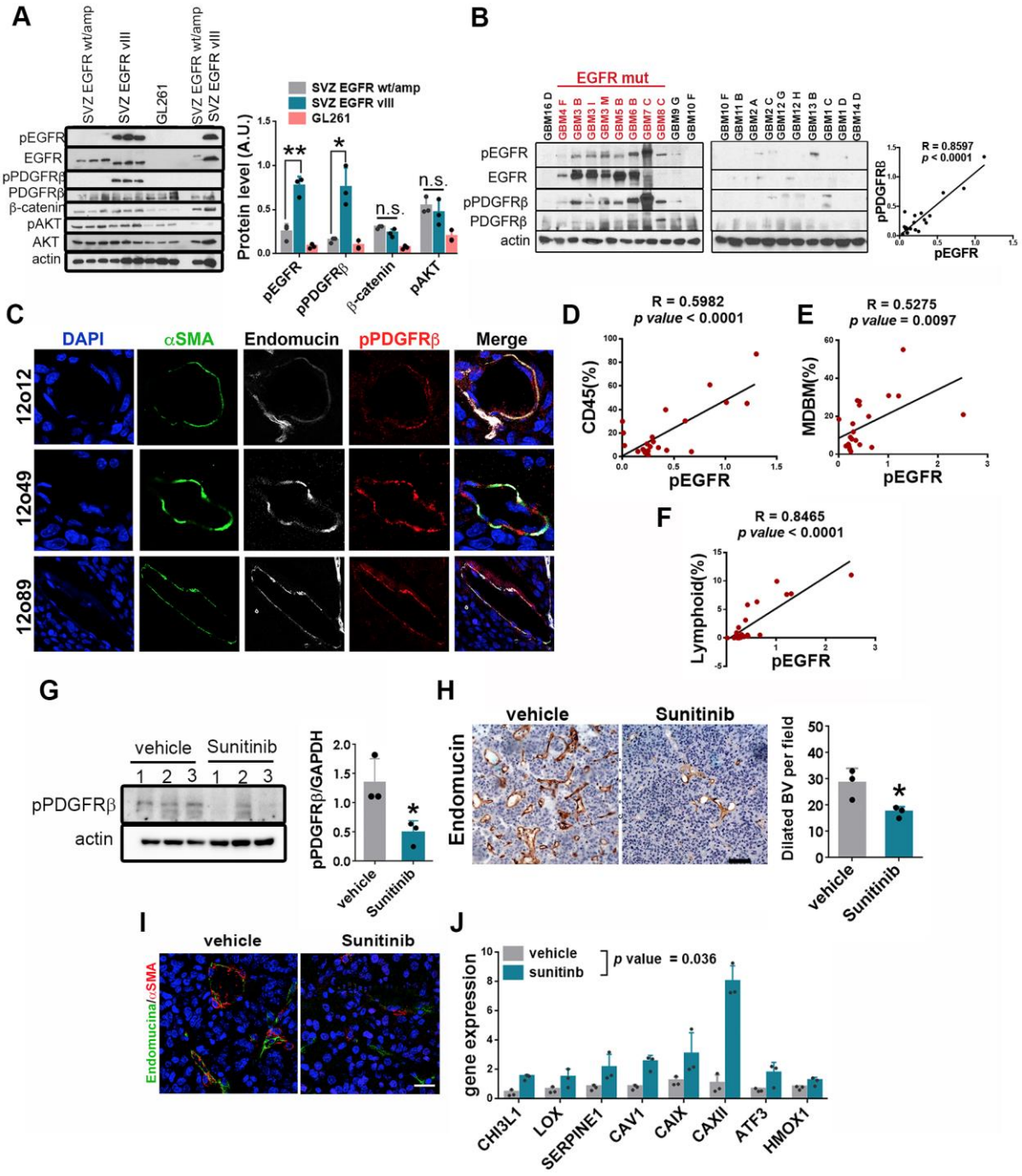

Supplementary Fig. 7. PDGFRβ signaling is activated in the blood vessels of mutant EGFR gliomas and stabilized the vasculature. (A) WB analysis and quantification of EGFR, pEGFR, PDGFRβ, pPDGFRβ, pAKT, AKT and β-Catenin in SVZ and GL261 tumors. Extracts from SVZ cells were loaded on the right as controls. Actin was used for normalization. **(B)** WB analysis of EGFR, pEGFR, PDGFRβ, pPDGFRβ in PDXs. GAPDH was used for normalization. Correlation between pEGFR and pPDGFRβ in shown on the right. **(C)**

Representative images of the IF analysis of αSMA, endomucin and pPDGFRβ in sections from mutant EGFR PDXs. **(D-F)** Correlation between the percentage of leukocytes (D), myeloid cells (E) and lymphocytes (F) in dissociated samples (flow cytometry analyses) and the levels of phospho-EGFR (WB analyses) in the same tumors. **(G)** WB analysis and quantification of pPDGFRβ in intracranial SVZ-EGFRvIII tumors treated with vehicle or sunitinib (6mg/kg/day). Actin was using for normalization. **(H)** Representative images of endomucin IHC staining in SVZ-EGFVRvIII tumors. Quantification of the number of dilated blood vessels (BVs) is shown on the right (n=3). **(I)** qRT-PCR analysis of hypoxic-related genes in the tumors in SVZ-EGFVRvIII tumors (n=3). *Actin* was used for normalization. n.s. not significant; *P ≤ 0.05; **P ≤ 0.01. Scale bars: 10 μm (C), 25 μm (I).

Supplementary Materials and Methods

Lentiviral/retroviral production

Lentiviral and retroviral particles were produced in 293T cells with packaging plasmid pCMVdR8.74 (Addgene #Plasmid 22036) and VSV-G envelope protein plasmid pMD2G (Addgene #Plasmid 12259) using Lipofectamine and Plus reagent (Invitrogen).

In vitro assays

For the time-course experiments, cells were starved for two hours in the presence of 5 µM ibrutinib or DMSO before adding 100 ng/µl of EGF. Cells were collected at 0, 10, 30 and 240 min before being chilled on ice and pelleted for WB. For MG132 (Millipore) treatment, 10 µM MG132 was added to the cells and collected 3 h after. Pellets were obtained for WB analysis. To test the viability of SVZ cells, 10000 cells grown in a 96-well microplate were incubated in the presence of dacomitinib (Pfizer, PF-299804) or vehicle (DMSO) for three days and cell viability was assessed by a colorimetric assay using a WST-1 reagent (Roche) according to manufacturer´s instructions.

Intracraneal tumor formation

Intracraneal orthotopic xeno- and allo-grafts were performed using a Hamilton syringe to inject 100.000-300.000 cells (resuspended in 2 µl of stem cell medium) into athymic Nude-Foxn1nu brains (Harlan Iberica). The injections were made into the striatum (coordinates: A–P, −0.5 mm; M–L, +2 mm, D–V, −3 mm; related to Bregma) using a Stoelting Stereotaxic device. When applicable, tumor growth was monitored in an IVIS equipment (Perkin Elmer) after intraperitoneal injection of D-luciferin (75 mg/Kg) (PerkinElmer). The animals were sacrificed at the onset of symptoms.

Heterotopic allografts

SVZ-EGFRwt/amp and SVZ-EGFRvIII cells (1×10^6) were resuspended in culture media and Matrigel (BD) (1:10) and then subcutaneously injected into nude mice. When tumors reached a visible size the tumor volume was measured with a caliper every 5 days. Tumor volume = 1/2(length × width2).

Mouse magnetic resonance imaging (MRI) and quantification

Global shimming was first performed and three scout images in axial, sagittal, and coronal direction were acquired using a T1 weighted spin echo sequence with a repetition time of 2.1 s and an effective echo time of 62 ms. The field of view (FOV) was of 3.0x3.0 cm^2, the thickness of the slices was 2.0 mm and the matrix size was 256x128, with a total acquisition time of 33 s. Then respiratory-gated T1-weighted spin echo images in coronal orientation were acquired

for the tumor visualization with the next parameters: TR/TE = 505/10 ms; FOV=2.56x2.56 cm^2; slice thickness: 1.0 mm; number of slices: 9; number of signal averages = 4; matrix size: 256x192. Data were zero filled to obtain images of 256x256 pixels. The MRI images obtained were analyzed with the ImageJ software. Images were acquired Pre-gadolinium injection and 10-, 25-, 45-, 65-, 90- and 115-minutes Post-gadolinium injection. In vivo Pre- and Post- images were analyzed using ImageJ software (National Institutes of Health, Bethesda, Maryland). The intensity signal was measured in regions of interest, tumor region (I_t), contralateral region (I_c) and an area outside the mouse (I_{noise}). The Signal-to-noise ratio (SNR) of the region of interest were measured for each slice and time point and it is defined by $SNR_{(t)}=I_t/I_{noise}$, for the tumor region, and $SNR_{(c)}=I_c/I_{noise}$ for the contralateral region. The normalized enhancement ratio (NER%) of the tumor region to the contralateral region was calculated as $\%NER_t = \left[\left\{(SNR_t/SNR_c)_{post} - (SNR_t/SNR_c)_{pre}\right\}/(SNR_t/SNR_c)_{pre}\right] \times 100$.

Determination of BBB integrity with Evans Blue extravasation

For Evans blue infusion, 2ml/kg of Evans blue (E-2129, Sigma-Aldrich, MO) (2% dilution in PBS) was injected intravenously into the tail vein. After 30 min, the mice were deeply anesthetized with isoflurane and transcardially perfused in the heart beating through the left ventricle with 50 ml of ice-cold PB 0.1M followed by 50 ml of ice-cold 4% paraformaldehyde (PFA) in PB 0.1M. Brains were dissected afterwards.

Chicken chorioallantoic membrane (CAM) assay

For in vivo evaluation of the angiogenic inductive potential of SVZ derived CM, a CAM assay was performed as previously reported (Casas et al., 2018). Briefly, fertilized chicken eggs (Agricola Chorombo, Chile) were incubated at 38.5 °C with constant humidity. At embryonic day 1 (E1), 3 mL of albumin was extracted from each egg; a round window (2 cm2) was created on E4. A Bio-cellulose scaffold of 6mm of diameter was filled with 100 µl of medium to be assed: CM from SVZ-EGFRwt/amp or SVZ-EGFRvII, culture media (as negative control) and 100 µg VEGFA (positive control). On E8, the CAM vasculature was photographed; subsequently, each experimental condition scaffold was placed on top of the CAM; for each condition 14 eggs from different batches were used. On day E12, white cream was injected under the CAM before photographing every egg, in order to improve the visualization of the vessels.

Inmunofluorescent (IF) and Inmunohistochemical (IHC) staining

For immunostaining analyses, intracraneal tumors as well as human samples were fixed with 4% PFA for 12h at 4ªC and then tumors were embedded in paraffin. Paraffin sections (5 µM) were obtained with a microtome. Some animals were injected intraperitoneally with BrdU

(Sigma Aldrich) (50mg/Kg) in saline solution 2 h before being sacrificed. Paraffin sections were incubated with primary antibodies (Supplementary Table S2) O/N at 4ºC. To detect BrdU, the paraffin sections were pre-incubated with heated 2N HCl for 15 min following by incubation in 0.1 M sodium borate [pH 8.5] during 10 min. The second day, sections were incubated with the appropriate secondary antibody. For IF, fluorescent antibodies (1:200 dilution) were used for 2h at room temperature. Prior to coverslip application, nuclei were counterstained with DAPI and imaging was done with Leica SP-5 confocal microscope. For IHC, sections were incubated with HRP conjugated antibodies (1:200 dilution) (Supplementary Table S2). Target proteins were detected with the ABC Kit and the DAB kit (Vector Laboratories).

Western Blot analysis

Protein extracts were prepared by re-suspending cell pellets or tumor tissue samples in lysis buffer (50 mM Tris (pH 7.5), 300 mM NaCl, 0.5% SDS, and 1% Triton X-100) and incubating the cells for 15 min at 100º. The lysed extracts were centrifuged at 13,000 g for 10 min at room temperature and the protein concentration was determined using a commercially available colorimetric assay (BCA Protein Assay Kit). Approximately 20 to 30 µg of protein were resolved by 10% or 12% SDS-PAGE and they were then transferred to a nitrocellulose membrane (Hybond-ECL, Amersham Biosciences). The membranes were blocked for 1 h at room temperature in TBS-T (10 mM Tris-HCl [pH 7.5], 100 mM NaCl, and 0.1% Tween-20) with 5% skimmed milk, and then incubated overnight at 4ºC with the corresponding primary antibody (Supplementary Table 2) diluted in TBS-T. Then, the membranes were incubated for 2 h at room temperature with their corresponding secondary antibody (HRP-conjugated anti mouse or anti rabbit, DAKO) diluted in TBS-T. Proteins were visible by enhanced chemiluminiscence with ECL (Pierce) using Amersham imager 680 and the signal was quantified by Fiji-ImageJ software.

Quantitative reverse-transcriptase PCR (qRT-PCR)

RNA was extracted from the tissue or the cell pellets using RNA isolation Kit (Roche) and it was digested with DNase I (Roche) according to the manufacturer's instructions. cDNA was synthesized with SuperScript II Reverse Transcriptase (Takara). qRT-PCR reactions were performed using the Light Cycler 1.5 (Roche) with the SYBR Premix Ex Taq (Takara). The primers used for each reaction are indicated in Supplementary Table S3. Gene expression was quantified by the double delta Ct method.

Supplementary Table 1. List of GBM cell lines. The table indicates the genetic status of *EGFR* of the different primary GBM cell lines used in this study. (nd: not determined. 0: not present. 1: present)

Cell line	Origin	EGFR amp	EGFR mut
GBM1	Hospital 12 de Octubre	1	0
GBM2	Hospital 12 de Octubre	0	0
GBM3	Hospital 12 de Octubre	1	1 (EGFR vIII)
GBM4	Hospital 12 de Octubre	1	1 (EGFR vIII)
GBM5	Hospital 12 de Octubre	1	1 (EGFR vIII)
GBM6	Hospital 12 de Octubre	1	1 (EGFR vIII)
GBM7	Hospital 12 de Octubre	0	1 (V774M)
GBM8	Hospital 12 de Octubre	0	1
GBM9	Hospital 12 de Octubre	nd	nd
GBM10	Hospital 12 de Octubre	nd	nd
GBM11	Hospital 12 de Octubre	nd	nd
GBM12	Hospital 12 de Octubre	nd	nd
GBM13	Hospital 12 de Octubre	nd	nd
GBM14	Hospital 12 de Octubre	0	0
GBM15	Hospital 12 de Octubre	nd	nd
GBM16	Hospital 12 de Octubre	1	0

Supplementary Table S2. Antibodies used for western-blot (WB), immunohistochemistry (IHC), immunofluorescence (IF) and flow-cytometry (FC) analysis.

Antibody	Dilution	Source
α-SMA	1:500 (WB), 1:100 (IHC)	Santa Cruz Biotechnology
β-Actin	1:1000 (WB)	Sigma
BrdU	1:100	Dako
AKT	1:1000 (WB)	Cell Signaling
CD248	1:500 (WB), 1:100 (IF)	Santa Cruz Biotechnology, BDBiosciences
CD34	1:100 (IF)	Leica
CD3-vg	1:20 (FC)	Beckton Dickinson
CD11b-647	1:40 (FC)	Miltenyi
CD45	1:100 (IHC)	eBioscience
CD45-488	1:40 (FC)	Miltenyi
CD49d-percy5	1:100(IF)	BioLegend
CD68- 488	1:100 (IF)	BioRad
EGFR	1:1000 (WB)	Cell Signaling
EGFR vIII	1:1000 (WB)	Cell Signaling
Endomucin	1:100 (IF)	Santa Cruz Biotechnology
GAPDH	1:500 (WB)	Santa Cruz Biotechnology
GFP	1:100 (IF)	Santa Cruz Biotechnology
HIF1α	1:500 (WB)	Santa Cruz Biotechnology
p-AKT	1:1000 (WB)	Cell Signaling
p-BMX	1:1000 (WB)	Invitrogen
p-EGFR	1:1000 (WB)	Cell Signailing
p-ERK	1:500 (WB)	Santa Cruz Biotechnology
p-SRC	1:1000 (WB)	Cell Signaling
p-STAT3	1:1000 (WB)	Cell Signaling
SOX9	1:1000(WB)	Cell Signaling
p-SOX9	1:1000 (WB)	Abcam
Cy3 anti- mouse	1:200 (IF)	Jackson Immunoresearch
Cy3 anti-rabbit	1:200 (IF)	Jackson Immunoresearch

Cy5 anti-mouse	1:200 (IF)	Jackson Immunoresearch
Cy5 anti-rabbit	1:200 (IF)	Jackson Immunoresearch
Cy5-anti rat	1:200 (IF)	Jackson Immunoresearch
HRP anti-mouse	1:5000 (WB), 1:1000(IHC)	GE Healthcare
HRP anti-rabbit	1:5000 (WB), 1:1000(IHC)	Santa Cruz Biotechnology
HRP anti-rabbit	1:5000 (WB), 1:1000(IHC)	Cell Signaling

Supplementary Table S3. Primers used for the qRT-PCR analysis.

Species	Gene	Forward (5'-3´)	Reverse (5'-3´)
mouse	**CD31**	TCCAGGTGTGCGAAATGCT	TGGCAGCTGATGCCTATGG
	VE-CAD	TTACTCAATCCACATACACATTTTCG	GCATGATGCTGTACTTGGTCATC
	CD248	TTGATGGCACCTGGACAGAGGA	TCCAGGTGCAATCTCTGAGGCT
	αSMA	ACCATCGGCAATGAGCGTTTCC	GCTGTTGTAGGTGGTCTCATGG
	PDGFRB	CCGGAACAAACACACCTTCT	TATCCATGTAGCCACCGTCA
	MMP9	GCAAGGGGCCGTGTCTGGAGATTC	GCCCACGTCGTCCACCTGGTT
	LMNA	TTGCCTCAACTGCAATGACAA	TCTCGATGTCGGTAAAACCCC
	VEGFR1	TTTGGCAAATACAACCCTTCAGA	GCAGAAGATACTGTCACCACC
	VEGFR2	CATCACCGAGAACAAGAACAAAACT	GATACCTAGCGCAAAGAGACACATT
	TEK	ACGGACCATGAAGATGCGTCAACA	TCACATCTCCGAACAATCAGCCTGG
	EPHA2	GCACAGGGAAAGGAAGTTGTT	CATGTAGATAGGCATGTCGTCC
	AQP1	AGGCTTCAATTACCCACTGGA	GTGAGCACCGCTGATGTGA
	VEGF A	TGCCAAGTGGTCCCAGGCTGC	CCTGCACAGCGCATCAGCGG
	PDGF A	GATACCTCGCCCATGTTCTG	CAGGCTGGTGTCCAAAGAAT
	PDGF B	GGGCCCGGAGTCGGCATGAA	AGCTCAGCCCCATCTTCATCTTACGG
	PGF	GAGGCCAGAAAGTCAGGGGGC	ATGGGCCGACAGTAGCTGCGA
	NG2	GACGGCGCACACACTTCTC	TGTTGTGATGGGCTTGTCAT
	End	TGCACTTGGCCTACGACTC	TGGAGGTAAGGGATGGTAGCA
	Pi3kca	GCTCTTCGCCATCACACAAAC	GGCATTCCTGTCATCAGCATC
	Cxcr4	GACTGGCATAGTCGGCAATGGA	CAAAGAGGAGGTCAGCCACTGA
	Cx45	ACTCCCTCTGTGATGTACCTGG	GTGCTGTTTCCAACGCATGGCA
	Timp1	TCTTGGTTCCCTGGCGTACTCT	GTGAGTGTCACTCTCCAGTTTGC
	Chi3l1	GCTTTGCCAACATCAGCAGCGA	AGGAGGGTCTTCAGGTTGGTGT
	Lox	CATCGGACTTCTTACCAAGCCG	GGCATCAAGCAGGTCATAGTGG
	Serpine1	CCTCTTCCACAAGTCTGATGGC	GCAGTTCCACAACGTCATACTCG
	Cav1	CACACCAAGGAGATTGACCTGG	CCTTCCAGATGCCGTCGAAACT
	Car9	GGCGAACGATTGAGGCTTCCTT	GCTGGTGACAGCAAAGAGAAGG
	Car12	TGGCTCTGAACACACCGTGAGT	TTGTCACTGGCGGTGCTGAAGT
	Atf3	GAAGATGAGAGGAAAAGGAGGCG	GCTCAGCATTCACACTCTCCAG
	Hmox1	CACTCTGGAGATGACACCTGAG	GTGTTCCTCTGTCAGCATCACC
human	**αSMA**	TAGCACCCAGCACCATGAAGATCA	GAAGCATTTGCGGTGGACAATGGA
	NG2	AGCTCTACTCTGGACGCC	ATCGACTGACAACGTGGC
	CD248	AGACCACCACTCATTTGCCTGGAA	AGTTGGGATAATGGGAAGCGTGGT
	PDGFRB	ACGGCTCTACATCTTTGTGCCAGA	TCGGCATGGAATGGTGATCTCAGT
	SERPINE	CATAGTGGAAGTGATAGAT	ACTCTGTTAATTCGTCTT
	CD34	CCTCAGTGTCTACTGCTGGTCT	GGAATAGCTCTGGTGGCTTGCA
	VEGFA	CTAACACTCAGCTCTGCCC	ACACACAAATACAAGTTGCCAA
	ANGPT2	ATTCAGCGACGTGAGGATGGCA	GCACATAGCGTTGCTGATTAGTC
	IGFBP2	CGAGGGCACTTGTGAGAAGCG	TGTTCATGGTGCTGTCCACGTG
	CHI3L1	CCACAGTCCATAGAATCCTCGG	TGCCTGTCCTTCAGGTACTGCA
	LOX	GATACGGCACTGGCTACTTCCA	GCCAGACAGTTTTCCTCCGCC
	CAV1	CCAAGGAGATCGACCTGGTCAA	GCCGTCAAAACTGTGTGTCCCT
	CAIX	GTGCCTATGAGCAGTTGCTGTC	AAGTAGCGGCTGAAGTCAGAGG
	CAXII	GACCTTTATCCTGACGCCAGCA	CATAGGACGGATTGAAGGAGCC
	ATF3	CGCTGGAATCAGTCACTGTCAG	CTTGTTTCGGCACTTTGCAGCTG
	HMOX	CCAGGCAGAGAATGCTGAGTTC	AAGACTGGGCTCTCCTTGTTGC
	CD31	AAGTGGAGTCCAGCCGCATATC	ATGGAGCAGGACAGGTTCAGTC
	END	GCAAGCACTTCAGCAACCAGCC	GGATCTGCCTTCCAGCACATTC
	SOX9	AGGAAGCTCGCGGACCAGTAC	GGTGGTCCTTCTTGTGCTGCAC